HORIZON EUROPE PROGRAMME
HORIZON-JTI-CLEANH2-2024

GA No. 101192342

Direct seawater electrolysis technology for distributed hydrogen production

SWEETHY

SWEETHY – Deliverable report

D3.2 – Catalysts screening in seawater

Clean Hydrogen Partnership

Co-funded by the European Union

Deliverable No.	D3.2	
Related WP	WP3	
Deliverable Title	Catalysts screening in seawater	
Deliverable Date	2026-02-28	
Deliverable Type	Report	
Dissemination level	Public (PU)	
Author(s)	Sabrina C. Zignani (CNR), Mariarosaria Pascale (CNR), Marta Fazio (CNR), Nicola Briguglio (CNR), Bryan Mondello (CNR), Antonino S. Aricò (CNR) Carmen Tébar Soler (CIDETEC), Aliona Nicolenco (CIDETEC), Francisco Alcaide (CIDETEC) Erlind Mysliu, Yejung Choi (SINTEF)	2026-02-20
Checked by	Antonino S. Aricò	2026-02-21
Reviewed by	Olesia Danyliv (RISE)	2026-02-24
Approved by	Olesia Danyliv (RISE)	2026-02-24
Status	Final	2026-02-28

Deliverable Summary

SWEETHY develops an advanced technology for direct seawater electrolysis that is able to produce H_2 and O_2 under intermittent conditions accounting for the coupling to renewable power sources (especially wind, PV). The electrolyser design is based on an anion exchange membrane (AEM) fed with alkaline seawater. The SWEETHY technology is developed along three dimensions:

a) Materials optimisation. To meet the specific requirement of seawater environment and cost effectiveness the project will focus on corrosion resistance and selective PGM-free electrocatalysts for hydrogen and oxygen evolution reactions, on AEM membranes with high selectivity for transporting hydroxide anions and anti-fouling properties as well as on novel anti-corrosion coatings for bipolar plates and porous transport layers.

b) Electrolyser stack prototyping. The project will exploit a novel stack architecture, which uses hydraulic cell compression to host the advanced materials and to produce H_2 at high pressure.

c) Sustainability analysis. The project will conduct studies (life-cycle assessment (LCA), techno-economic analysis (TEA)) to evaluate circularity of the materials and electrolyser system and its integration into renewable power systems and to explore an efficient by-product utilisation way through industrial symbioses.

Combining these three dimensions, SWEETHY will utilise Mediterranean seawater from the coast of Messina, Italy, to test its electrolyser with the goal withstand more than 2000 h of operation to produce 20 g_{H2}/h with a degradation rate lower than 1%/100h. In addition, SWEETHY will demonstrate how the operation of the electrolyser can ensure an optimised revenue concerning by-products and grid services.

Deliverable 3.2, "Catalysts Screening in Seawater," reports the progress and key results achieved up to Month 12 (M12) within Work Package 3 (WP3), which focuses on the evaluation of the electrocatalysts for the hydrogen evolution reaction (HER) and oxygen evolution reaction (OER) under conditions relevant to direct seawater electrolysis. This deliverable provides an overview of the experimental activities carried out by the WP3 partners CNR (Consiglio Nazionale Delle Ricerche, Italy), CIDETEC (Fundacion CIDETEC), and SINTEF (SINTEF AS), which includes the screening and performance assessment of metal powder electrocatalysts tested in both single-cell and half-cell configurations. The results obtained in seawater-based electrolytes are discussed in terms of activity, stability, and suitability for operation under realistic electrolysis conditions, thereby contributing to the identification of promising catalyst candidates for further development.

Contents

List of Figures

List of Tables

1 Introduction

The direct use of seawater in electrolysis systems introduces several relevant challenges widely recognized yet still unresolved, when compared to systems operating with purified water. The high contents of salts and the ionic composition of seawater enhance corrosive phenomena, negatively affecting electrolyser components. In addition, the presence of suspended solids, mineral deposits, and biological contaminants may cause physical obstructions, either by covering catalytic active sites or by impairing the integrity of separator materials. At the anode, a critical issue arises from the competition between the oxygen evolution (OER) and chlorine evolution reactions. The presence of organic contaminants can affect the purity of the produced H_2 and may cause cathode poisoning. Furthermore, significant pH variations occurring during both the hydrogen evolution reaction (HER) and OER accelerate catalyst degradation and trigger unwanted side reactions. These combined effects lead to reduced system efficiency lowering hydrogen production for the same energy consumption and impact the electrolyser durability. Identifying complementary revenue streams such as the exploitation of valuable by-products is essential to improve the economic feasibility of direct seawater electrolysis. Therefore, the SWEETHY project is designed to tackle all the challenges outlined above. Its primary objective is to develop innovative solutions encompassing advanced materials, optimized components, and improved system architectures. The electrocatalysts developed within the project aim at delivering high efficiency, robust performance, and long-term durability while avoiding or minimizing the use of PGM- and CRM-based components. This strategy supports enhanced circularity by limiting the reliance on primary raw materials.

Deliverable 3.2, “Catalysts Screening in Seawater,” provides an update on the progress and principal outcomes achieved by Month 12 (M12) within Work Package 3 (WP3). These are specifically concerning the evaluation of electrocatalysts in synthetic and natural seawater environments. The document focuses on assessing electro-catalysts’ performance for both hydrogen evolution reaction (HER) and oxygen evolution reaction (OER) under conditions representative of direct seawater electrolysis or in the presence of real seawater from the coast of Messina (Italy). This deliverable provides an overview of the experimental activities conducted by the WP3 partners, i.e., CNR, CIDETEC, and SINTEF, including electrochemical screening, benchmarking, and performance characterisation of the selected electrocatalysts. Electrochemical tests were carried out using both half-cell and single-cell configurations to generate a dataset useful for screening. Whereas catalyst down-selection will be made after the durability tests that will be reported in D3.3 due in M16 (June 2026) of the project.

In this deliverable report, the results obtained in seawater-based electrolytes are analysed in terms of catalytic activity, short-term operational stability and related degradation behaviour, and overall suitability for seawater electrolysis. These findings support the identification of promising catalyst formulations that will be down selected for further optimisation and scale-up within the project.

2 Results and discussion

2.1 Electrolyte solution: 1 M KOH in natural or synthetic seawater

Natural seawater was collected directly from the Mediterranean Sea of Messina, Sicily (10m far from the beach) and used as received. The main composition of the seawater collected in Messina is following: 77.8 % NaCl, 9.7% MgCl2, 6.1 % MgSO4, 4.1% CaSO4, 2.1 % KCl, 0.2 % NaBr, and its main characteristics were reported in reference [1].

Synthetic seawater was prepared according to the harmonised protocol for synthetic seawater preparation developed within the SWEETHY-project [2].

Potassium hydroxide (KOH, analytical grade) pellets were added to the real or synthetic seawater under continuous stirring to obtain a final concentration of 1 M. The addition of KOH resulted in an immediate visual change of the solution, with the formation of a white, turbid suspension. This instantaneous precipitation is attributed to the reaction between the highly alkaline environment and divalent cations naturally present in seawater, primarily Mg^{2+} and Ca^{2+}, leading to the formation of poorly soluble hydroxide species. After KOH addition, the supernatant suspension was collected and recirculated at room temperature to ensure homogeneous conditions. The chemical composition of the pristine seawater and the KOH + seawater electrolyte was analysed by inductively coupled plasma (ICP) spectroscopy (Figure 1). As shown in Figure 1, the concentration of magnesium was drastically reduced after KOH addition, confirming its rapid precipitation, while calcium showed a partial decrease. Other elements, such as sodium and potassium, decreased in content. These results are consistent with the expected selective precipitation of alkaline earth metals under strongly alkaline conditions.

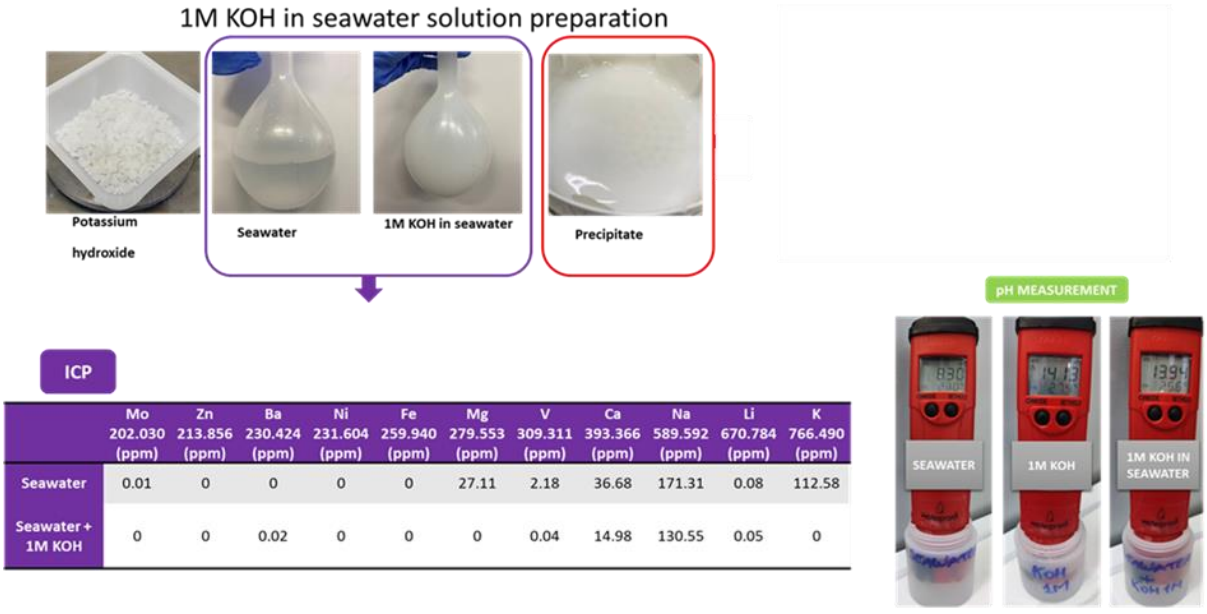

	Mo 202.030 (ppm)	Zn 213.856 (ppm)	Ba 230.424 (ppm)	Ni 231.604 (ppm)	Fe 259.940 (ppm)	Mg 279.553 (ppm)	V 309.311 (ppm)	Ca 393.366 (ppm)	Na 589.592 (ppm)	Li 670.784 (ppm)	K 766.490 (ppm)
Seawater	0.01	0	0	0	0	27.11	2.18	36.68	171.31	0.08	112.58
Seawater + 1M KOH	0	0	0.02	0	0	0	0.04	14.98	130.55	0.05	0

Figure 1. Preparation of the 1 M KOH electrolyte in natural seawater. The addition of KOH induces instantaneous precipitation of Mg^{2+} and partial precipitation of Ca^{2+}, forming a turbid suspension. The ICP analysis confirms the change in ion concentrations and the pH measurement shows the corresponding values of the measured samples.

The pH of the solutions was measured using a calibrated pH meter and corrected. Pristine seawater exhibited a pH 8.3, whereas the 1M KOH + seawater electrolyte reached highly alkaline values, around pH 14, comparable to those of a reference 1M KOH solution prepared in deionised water. The combination of visual inspection, ICP analysis, and pH measurements confirms that the preparation of alkaline electrolytes directly in natural seawater leads to immediate salt precipitation and significant modification of the ionic composition.

2.2 Electrocatalysts

Table 1 summarises all electrocatalysts prepared by **CNR, CIDETEC, and SINTEF**, along with the commercial materials used in this deliverable. The commercial catalysts Co_3O_4 and Pt/C (40 wt%) were used as received. Co_3O_4 displays the typical cubic spinel structure (Fd-3m), whereas the Pt nanoparticles supported on carbon exhibit a face-centered cubic (fcc) structure with an average particle size of 3.8 nm.

Among the catalysts synthesised by CNR, the NiMo/KB material was produced via co-precipitation, yielding nanostructured Ni and Mo phases supported on Ketjenblack carbon. Nickel crystallises in the fcc structure, while molybdenum adopts a bcc nanocrystalline structure, with an overall particle size of about 22 nm. The NiFe LDH catalyst, also synthesised by CNR using co-precipitation, presents the typical rhombohedral layered double hydroxide (LDH) structure, forming nanosheet-like morphologies with an average particle size of 4.6 nm.

The catalysts developed by **SINTEF** include two types of NanoPTL (nanoporous, template-less Ni structures). The first, NanoPTL@Ni_3S_2, is obtained by magnetic field assisted chemical reduction followed by hydrothermal sulfidation, which generates a rhombohedral Ni_3S_2 shell surrounding an fcc Ni core. The resulting wire-like structures have thicknesses ranging from 200 to 500 nm.
The second material, NanoPTL (Ni), is produced solely by magnetic field assisted chemical reduction. It consists of metallic Ni with an fcc structure, forming wire-like elements between 50 and 200 nm in thickness, decorated with Ni cones of approximately 20 nm.

CIDETEC has developed a broad range of catalysts based on Ni-S, Mo-S, Ni-Mo-S, and LDH systems, synthesised through hydrothermal routes, electrodeposition, or solid-solid methods. For example, NiS_2 crystallises in a cubic structure with particle sizes around 15 nm, while MoS_2 and $NiMoS_2$ display the typical hexagonal structure with particles of 5-6 nm. Some electrodeposited catalysts (Ni-Mo and Ni-Mo-S) exhibit an amorphous-like nature, which is consistent with the synthesis technique. LDH-based materials (NiFe-LDH and NiMn-LDH) show the expected hexagonal layered structure, with particle sizes from 5 to 12 nm. Finally, Ni-MoO_3, produced via solid-solid synthesis, crystallises in the orthorhombic MoO_3 phase, with particle sizes between 30 and 45 nm.

The physico-chemical characteristics of these materials have been reported in deliverable D3.1 [3].

Table 1. Summary of catalysts used in this study, including synthesis method, average particle size, and crystal structure

Catalysts	Synthesis method	Particle size (nm)	Structure
Co_3O_4	Commercial powder (Alfa Aesar)	35	Cubic spinel (Fd-3m)
Pt/C 40%	Commercial powder (Thermo Scientific)	3.8	Pt: face-centered cubic (fcc)

NiMo/KB (**CNR**)	Co-precipitation	22	Ni: fcc, Mo: bcc (nanocrystalline)
NiFe LDH (**CNR**)	Co-precipitation	4.6	Rhombohedral layered structure (LDH)
NanoPTL@Ni_3S_2 (**SINTEF**)	Magnetic field assisted chemical reduction followed by hydrothermal sulfidation	200-500 in wire thickness	Rhombohedral Ni3S2 shell on Ni core (fcc)
NanoPTL (**SINTEF**)	Magnetic field assisted chemical reduction	50-200 in wire thickness, decorated with 20 nm Ni cones	Face-centered cubic (fcc)
NiS_2 (**CIDETEC**)	Hydrothermal synthesis	15	Cubic
MoS_2 (**CIDETEC**)	Hydrothermal synthesis	5-6	Hexagonal
$NiMoS_2$ (**CIDETEC**)	Hydrothermal synthesis	5-6	Hexagonal MoS_2
Mo_2C (**CIDETEC**)	Solid-solid synthesis	21	Hexagonal
Ni-Mo (**CIDETEC**)	Electrodeposition	<5	Amorphous-like
Ni-Mo-S (**CIDETEC**)	Electrodeposition	<5	Amorphous-like
NiFe-LDH (**CIDETEC**)	Hydrothermal synthesis	5-7	Hexagonal LDH phase
NiMn-LDH (**CIDETEC**)	Hydrothermal synthesis	12	Hexagonal LDH phase
Ni-MoO_3 (**CIDETEC**)	Solid-solid synthesis	30-45	Orthorhombic MoO_3

2.3 Membrane Electrode Assembly and single-cell configuration at CNR

Membrane electrode assemblies (MEAs) were prepared by first formulating catalyst inks for the anode and cathode.

The inks were obtained by mixing an anion exchange ionomer, electrocatalyst powder, and solvent. A commercial PiperION® anionic ionomer (10 wt%) was used as the binder for ink preparation. The catalyst inks were dispersed in ethanol and sonicated for 30 min to ensure homogeneous dispersion prior to deposition. Catalyst layers were deposited by spray-coating onto the appropriate porous transport layers (PTLs). Different PTLs have been investigated including Pt coated Ti felt or Ni-felt from Bekaert, see [2]. During deposition, the substrates were placed on a heated plate to promote solvent evaporation, and a controlled distance between the airbrush and the support was maintained to prevent excessive ink penetration into the porous structure. Anode inks, based on catalysts in their oxidized form, were deposited onto dedicated PTLs, while cathode inks, containing catalysts in their reduced form, were spray-coated onto gas diffusion layers (GDLs) e.g. Sigracet; consisting of carbon paper (Sigracet 39BB) [2]. The resulting electrocatalyst loadings were approximately 3 mg cm^{-2} for the anode and 1 mg cm^{-2} for the cathode.

Prior to MEA assembly, the PiperION® membrane (thickness in the range of 40-60 µm and supplied in the hydroxide (OH^-) form) and the produced electrodes were immersed in a 1M KOH solution for 24 h

to ensure complete ion exchange and electrochemical activation. A cold assembly procedure (2.5 N m per tie rod cell compression) was then applied to the three components stacked in anode/ membrane/cathode to fabricate the MEAs. The cold assembly procedure was preferred to avoid potential thermal degradation of the membrane, which may occur during conventional hot press lamination.

The MEAs were assembled in a single cell housing composed of stainless-steel plates featuring a serpentine flow field design corresponding to an active area of 5 cm^2. Polytetrafluoroethylene (PTFE, Teflon®) gaskets were used to ensure proper sealing and to prevent electrolyte leakage. Cell compression was controlled at 2.5 N m per tie rod, ensuring intimate contact between the electrodes and the membrane, thereby forming a uniform sandwich like structure. The single cell was operated at 50 °C under atmospheric pressure. During all electrochemical measurements the anode compartment was supplied with 1M KOH at a flow rate of 10 mL min^{-1}, whereas Mediterranean seawater from the coast of Messina mixed with KOH or synthetic seawater mixed with 1M KOH was fed to the cathode, using a peristaltic pump. The operating temperature was maintained by heating mats applied to the external surfaces of the cell plates.

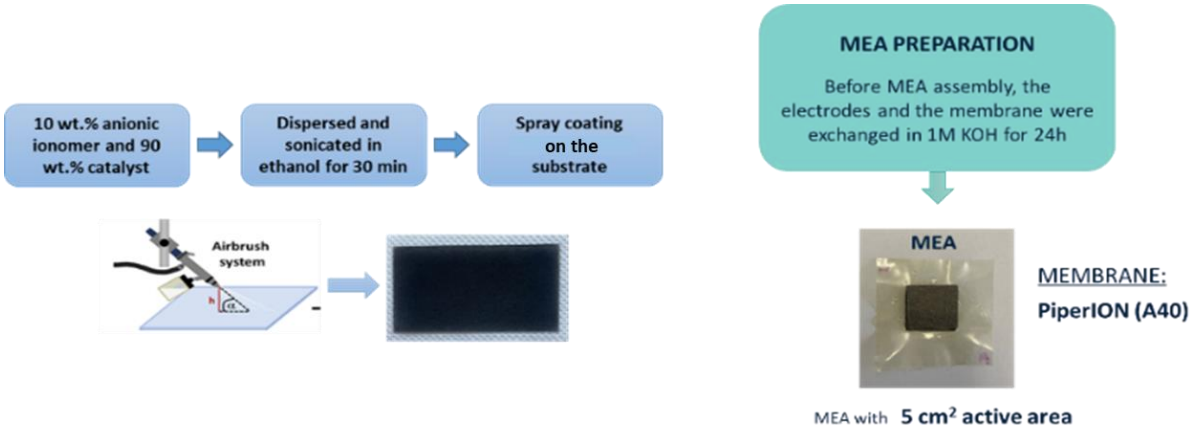

Figure 2. Schematic representation of the MEA fabrication process. Catalyst inks are spray-coated onto porous transport layers (anode) and gas diffusion layers (cathode). The electrodes are assembled with a PiperION® anion-exchange membrane using a cold-press procedure and mounted in a 5 cm^2 single cell.

2.4 Electrochemical Assessment at CNR

The electrochemical tests were performed using the MEA designated as MEA 6, 7, 8, 11, 12, 13 and 15 with different configurations, specified in Table 2. The electrochemical performance of the MEA was evaluated to assess reaction kinetics and overall cell behaviour under different operating conditions. The characterization was focused on determining the cell voltage response as a function of applied current density. To this end, galvanostatic polarization curves (cell voltage versus current density), galvanostatic durability tests (cell voltage versus time), and potentiostatic electrochemical impedance spectroscopy (EIS) measurements were performed. Polarization and chronopotentiometric measurements were conducted using a Keithley power supply system (Tektronix) and a PGSTAT Autolab 302 potentiostat/galvanostat (Metrohm) equipped with a 20 A current booster. EIS analyses were carried out using a frequency response analyzer (FRA). EIS measurements were performed under potentiostatic control over a frequency range from 1 MHz to 10 mHz, using single sine frequency

sweeping with ten points per decade. The amplitude of the applied sinusoidal perturbation was set to 10 mV (r.m.s.), ensuring operation within the linear response regime of the system. The ohmic (series) resistance (R_s) was determined from the high frequency intercept of the Nyquist plot with the real axis. The polarization resistance, encompassing both charge transfer and mass transport contributions, was estimated from the difference between the extrapolated low frequency and high frequency intercepts on the real axis.

Table 2. Summary of the membrane electrode assemblies (MEAs) investigated at CNR. The table reports the catalyst composition and support for both cathode and anode, ionomer percentage, catalyst loading on each electrode, and the ionomer and membrane type used in the MEA fabrication

MEA	Cathode	Ionomer (%)	Loading cathode (mg/cm²)	Anode	Ionomer (%)	Loading anode (mg/cm²)	Ionomer	Membrane	Filter anode	Filter cathode
6	NiMo/KB (CNR) on Sigracet	10	4.64	Co_3O_4 (Alfa Aesar) on Ni-felt	10	2.4	PiperION® (5%)	PiperION® A60	Titanium felt	Sigracet
7	40% Pt/C (Thermo scientific) on Sigracet	10	0.85	Co_3O_4 (Alfa Aesar) on Ni-felt	10	2.4	PiperION® (5%)	PiperION® A60	Titanium felt	Sigracet
8	NiMo/KB (**CNR**) on Sigracet	10	4.64	NiFe LDH (**CNR**) on Ni-felt	10	2.65	PiperION® (5%)	PiperION® A60	Titanium felt	Sigracet
11	40% Pt/C (Thermo scientific) on Sigracet	10	0.81	Co_3O_4 (Alfa Aesar) on Ti/Pt	10	2.67	PiperION® (5%)	PiperION® A40	Titanium felt	Sigracet
12	40% Pt/C (Thermo scientific) on Sigracet	10	0.81	Co_3O_4 (Alfa Aesar) on Ti/Pt	10	2.67	PiperION® (5%)	PiperION® A40	Titanium felt	Sigracet
13	40% Pt/C (Thermo scientific) on stainless steel	10	0.83	Co_3O_4 (Alfa Aesar) on Ti/Pt	10	2.67	PiperION® (5%)	PiperION® A40	Stainless steel	Titanium felt
15	40% Pt/C (Thermo scientific) on Sigracet	10	0.81	Co_3O_4 (Alfa Aesar) on Ti/Pt	10	2.55	PiperION® (5%)	PiperION® A40	Stainless steel	Sigracet

2.4.1 Electrochemical assessment of MEA 6, 7 and 8

Figure 3 shows the electrochemical performance of three membrane electrode assemblies (MEAs) operated with pure 1 M KOH on both anode and cathode sides at 50 °C. The anode and cathode catalyst combinations were: CoO_x |NiMo/KB (MEA 6), CoO_x | 40 wt% Pt/C (MEA 7), and NiFe-LDH | NiMo/KB (MEA 8).

Fig. 3 (a) reports the polarization curves before conditioning. Clear differences among the MEAs are observed over the whole current density range. MEA 8 exhibits the lowest cell voltage at a given

current density, followed by MEA 7, while MEA 6 shows the highest voltage. This trend indicates that replacing CoO_x with NiFe-LDH at the anode significantly improves cell performance, whereas the use of Pt/C instead of NiMo/KB at the cathode causes a decrease of efficiencies. The results suggest that, under pure 1M KOH electrolysis conditions, the anodic oxygen evolution reaction (OER) plays a significant role in determining overall cell efficiency. However, also the catalytic process of PGM-free catalysts affects efficiency as shown by the replacement of Pt with NiMo.

Fig. 3 (b) shows the conditioning step performed at 50 mA cm^{-2} for approximately 2 h. MEA 7 and MEA 8 display nearly constant cell voltages, with only minor fluctuations (<20 mV), indicating good stability and rapid electrochemical equilibration. In contrast, MEA 6 exhibits a small but noticeable voltage increase during conditioning, possibly related to slower interfacial activation or higher sensitivity to electrode wetting and contact resistances.

Fig. 3 (c) presents the polarization curves after conditioning. All MEAs showed an overall reduction in cell voltage compared to the pre-conditioning state, demonstrating the positive effect of the break-in procedure on electrode activation and ohmic resistance. Despite this general improvement, the relative performance rank remained unchanged. MEA 8 continued to deliver the best performance across the entire current density range, confirming the superior activity of the NiFe-LDH anode. MEA 7 showed intermediate behaviour, while MEA 6 remained the least efficient configuration.

These results highlight the strong influence of anode catalyst selection on alkaline electrolyzer performance and confirm that NiFe-LDH based anodes outperform CoO_x under the investigated operating conditions, both before and after conditioning.

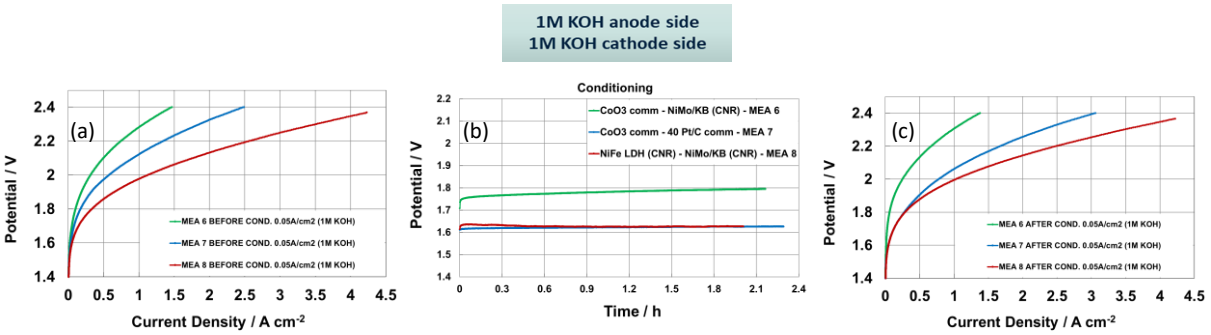

Figure 3. (a) Polarization curves of MEA 6, 7 and 8 recorded before conditioning, anode and cathode fed with 1M KOH. (b) Conditioning profiles at 50 mA cm^{-2} for ~2 h showing stabilization behaviour of the three MEAs. (c) Polarization curves after conditioning, highlighting performance improvement and permanent ranking MEA 8 > MEA 7 > MEA 6.

Figure 4 presents the electrochemical impedance spectroscopy (EIS) results of the three MEAs, all assembled with a PiperION® A60 membrane and operated in 1 M KOH on both anode and cathode sides, before and after the conditioning procedure.

Figure 4 (a) shows the Nyquist plots recorded before conditioning. All MEAs displayed a capacitive response characterized by a depressed semicircle, typical of charge-transfer controlled processes in alkaline electrolysis cells. The high-frequency intercept on the real axis is similar for all samples but slightly shifted depending on the MEA configuration, reflecting differences in the overall ohmic

contribution of the cell. Among the three samples, MEA 8 (NiFe-LDH | NiMo/KB) exhibits the smallest arc, indicating the lowest total impedance. MEA 7 (CoO_x | Pt/C) shows an intermediate behaviour, while MEA 6 (CoO_x | NiMo/KB) presented the largest semicircle, extending to higher values. This trend suggests increasing resistive and kinetic contributions from MEA 8 to MEA 6. This indicated a superior performance of Pt vs NiMo and NiFe vs Co_3O_4.

Figure 4 (b) reports the Nyquist plots after conditioning. A general reduction in impedance was observed for all MEAs, as evidenced by a slight leftward shift of the curves and a decrease in the semicircle size. This behaviour indicates an improvement in the electrochemical response following the conditioning step. Despite this overall decrease in impedance, the relative ordering among the MEAs remained unchanged. MEA 8 continued to show the lowest impedance, followed by MEA 7, whereas MEA 6 still exhibited the highest impedance and the broadest arc.

Since all MEAs employ the same PiperION® A60 membrane, the observed differences in impedance response are mainly attributed to the different electrocatalyst combinations and interfacial properties rather than to membrane-related effects. The EIS results are fully consistent with the polarization measurements, confirming the superior electrochemical performance of the NiFe-LDH based anode configuration both before and after conditioning.

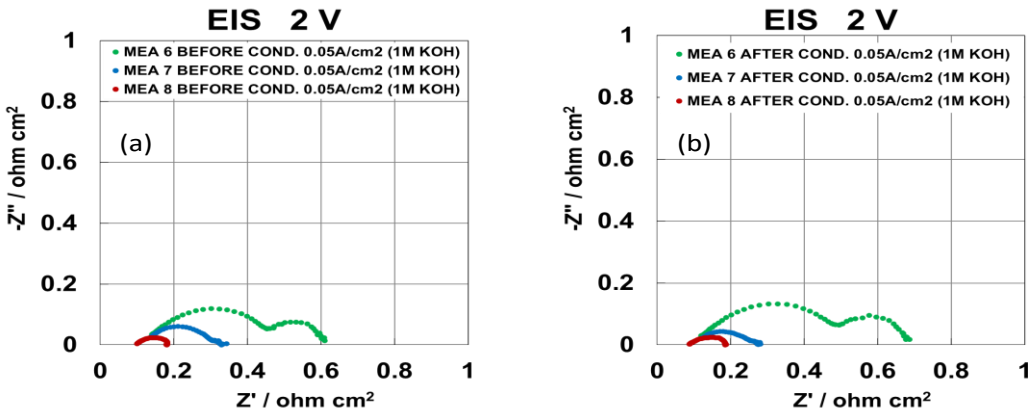

Figure 4. Nyquist plots of MEA 6, 7 and 8 measured at 2.0 V before (a) and after (b) conditioning in 1 M KOH.

Figure 5 shows the IR-free polarization curves of the three MEAs operated in 1 M KOH on both electrode sides, recorded before (a) and after (b) the conditioning procedure. The IR correction allows a direct comparison of the intrinsic electrode kinetics by eliminating the contribution of ohmic losses. Before conditioning (Figure 5(a)), clear differences among the MEAs are observed over the entire current density range. MEA 8 exhibited the lowest IR-free cell potential at a given current density, indicating the most favourable intrinsic electrocatalytic activity. MEA 7 showed intermediate behaviour, while MEA 6 required systematically higher potentials. The performance gap was already evident at low current densities and remained significant at higher currents, suggesting that the differences are mainly associated with kinetic limitations rather than ohmic contributions.

After conditioning (Figure 5(b)), all MEAs showed a modest but consistent improvement in IR-free performance, reflected by a slight downward shift of the cell voltages in the polarization curves. This behaviour indicates enhanced electrode activation and improved electrochemical utilization of the

catalyst layers following the break-in procedure. Despite this overall improvement, the relative ranking of the MEAs remains unchanged: MEA 8 continued to display the lowest IR-free potential, followed by MEA 7, while MEA 6 remained the least performant configuration.

The limited magnitude of the performance enhancement after conditioning, compared to the non-IR-corrected curves, suggests that the conditioning process mainly affects ohmic and interfacial resistances, while the intrinsic kinetic properties are largely preserved.

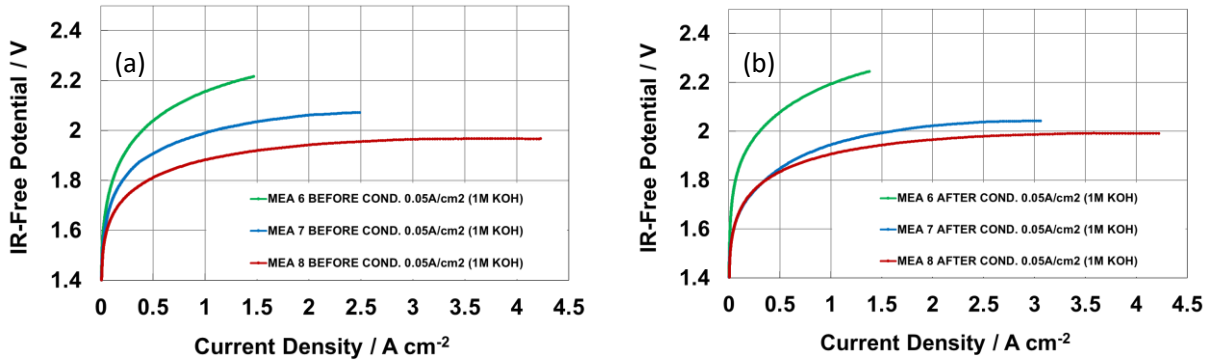

Figure 5. (a) IR-free polarization curves before conditioning of the MEAs 6,7,8. (b) IR-free curves after conditioning of the MEA 6,7,8.

Figure 6 shows the electrochemical performance of the same IR-free MEAs assembled with a PiperION® A60 membrane, tested with 1 M KOH at the anode and 1 M KOH in seawater at the cathode, at 50 °C.

Figure 6 (a) reports the polarization curves measured after conditioning in the seawater cathode configuration. All MEAs were able to operate stable over a wide current density range, indicating good compatibility of the PiperION® A60 membrane with seawater-based catholyte. However, compared to the fully alkaline configuration, higher cell voltages are observed, particularly at increasing current densities, reflecting the additional kinetic and mass-transport constraints associated with seawater operation. Among the three samples, MEA 8 (NiFe-LDH | NiMo/KB) again exhibits the lowest cell potential at a given current density, followed by MEA 7 (CoO_x | Pt/C), while MEA 6 (CoO_x | NiMo/KB) shows the highest overpotentials. The relative performance ranking is therefore preserved even under seawater cathode conditions.

Figure 6 (b) shows the short durability test performed at 0.5 A cm^{-2} for approximately 20 h. All MEAs demonstrate stable operation without abrupt voltage increases or signs of catastrophic degradation. MEA 8 displays the most stable voltage profile over time, with only minor fluctuations, indicating good interfacial stability and sustained catalytic activity under continuous operation. MEA 7 exhibits a slightly higher but still relatively stable cell voltage, while MEA 6 operates at the highest potential and shows more pronounced voltage variations. These differences suggest that catalyst selection and electrode architecture strongly influence long-term performance when seawater is used at the cathode.

Figure 6 (c) presents the polarization curves recorded after the durability test. Compared to the curves measured immediately after conditioning, no severe performance losses are observed for any MEA. The polarization behaviour remains largely unchanged, indicating that short-term operation in seawater does not significantly compromise the electrochemical performance of the cell. The relative ordering among the MEAs is maintained, with MEA 8 showing the best performance, followed by MEA 7, and MEA 6 remaining the least efficient configuration.
Overall, these results demonstrate the MEAs employing a PiperION® A60 membrane can operate reliably with seawater at the cathode, maintaining good performance and stability. The consistent superiority of the NiFe-LDH based anode highlights its robustness and effectiveness not only in fully alkaline conditions but also in more challenging seawater environments.

However, it is important to point out that its potential degradation by chlorides present in seawater is mitigated by the recirculation of 1M KOH at the anode.

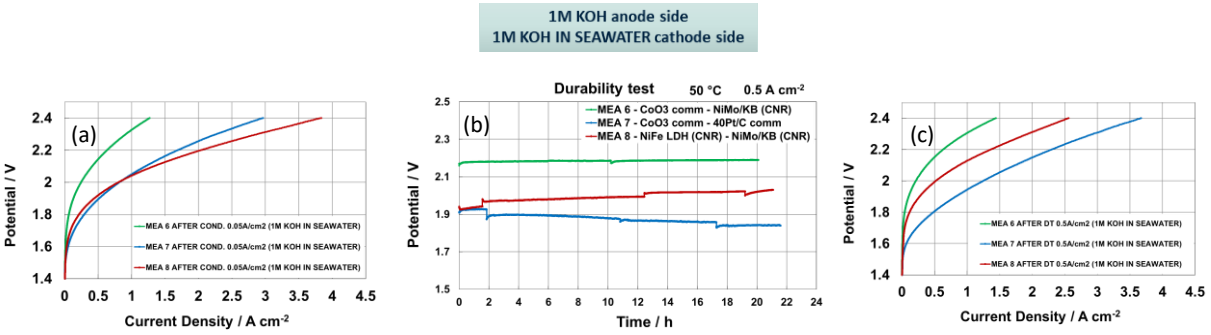

Figure 6. (a) Polarization curves after conditioning using 1 M KOH (anode) and 1 M KOH in seawater (cathode). (b) Short durability test at 0.5 A cm^{-2} (MEA 8 > MEA 7 > MEA 6). (c) Polarization curves recorded after the durability test.

Figure 7 shows the IR-free polarization curves of the MEAs operated with 1 M KOH at the anode and 1 M KOH prepared in seawater at the cathode, all employing a PiperION® A60 membrane. Curves were recorded after conditioning (a) and after the durability test at 0.5 A cm^{-2} (b). The IR correction removes the contribution of ohmic losses, allowing a direct comparison of the intrinsic electrode kinetics under seawater cathode conditions.

After conditioning (Figure 7 (a)), all MEAs displayed a smooth increase in IR-free potential with increasing current density, indicating stable kinetic behaviour despite the presence of seawater at the cathode. Differences among the MEAs are clearly visible over the whole current range. MEA 7 and MEA 8 exhibited lower IR-free potentials compared to MEA 6, particularly at low and intermediate current densities, while MEA 6 shows a steeper increase in potential. At higher current densities, the IR-free curves of MEA 7 and MEA 8 tend to converge, suggesting comparable intrinsic kinetic limitations under these conditions.

Figure 7 (b) reports the IR-free polarization curves measured after the durability test. No significant degradation of the IR-free performance was observed for any of the MEAs, indicating that the intrinsic catalytic activity is largely preserved during short-term operation with seawater at the cathode. MEA 7 exhibited the lowest IR-free potential over the investigated current density range, followed by MEA 8,

while MEA 6 remained the least performant configuration. Compared to the post-conditioning curves, only minor changes are detected, mainly at higher current densities.

Overall, the IR-free polarization curves demonstrate that the use of seawater at the cathode does not induce severe kinetic penalties for the MEAs. The relatively small differences between pre- and post-durability measurements suggest that performance variations observed in non-IR-corrected polarization curves are primarily associated with ohmic or interfacial effects rather than with intrinsic electrocatalytic degradation. These results confirm that the catalytic systems maintain stable kinetic behaviour under seawater cathode operation.

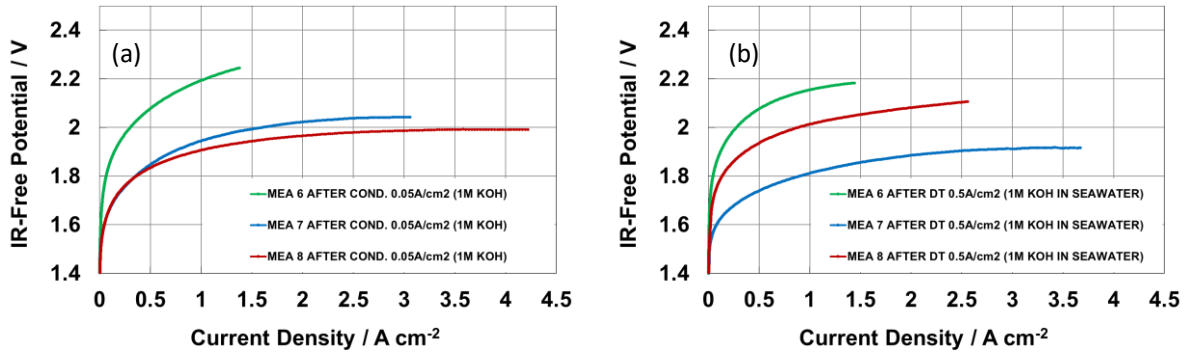

Figure 7. (a) IR-free polarization curves after conditioning with seawater catholyte of MEAs 6,7,8. b) IR-free curves after short durability test.

Figure 8 shows the Nyquist plots of the MEAs employing a PiperION® A60 membrane and operated with 1 M KOH at the anode and 1 M KOH in seawater at the cathode, recorded after conditioning and after a durability test at 0.5 A cm^{-2}. In both cases, all MEAs exhibited a depressed semicircle with a finite high-frequency intercept on the real axis, characteristic of a dominant charge-transfer process combined with ohmic contributions from the membrane, electrolyte, and cell contacts. After conditioning, MEA 8 displays the smallest semicircle and the lowest overall impedance, MEA 7 shows intermediate behaviour, and MEA 6 presents the largest arc extending to higher Z' values. Following the durability test, the overall shape of the impedance spectra remains largely unchanged, indicating stable electrochemical behaviour under seawater cathode operation. However, slight differences in semicircle size are observed: MEA 7 exhibits the lowest total impedance, MEA 8 shows a modest increase compared to the post-conditioning state, and MEA 6 continues to display the highest impedance. The high-frequency intercepts vary only marginally between the two measurements, while the main differences are associated with changes in the semicircle diameter. Overall, the EIS results indicate limited impedance evolution with time in seawater, with no evidence of abrupt degradation, and confirm that the relative electrochemical response of the MEAs is mainly governed by the electrode catalyst configuration rather than by membrane-related effects.

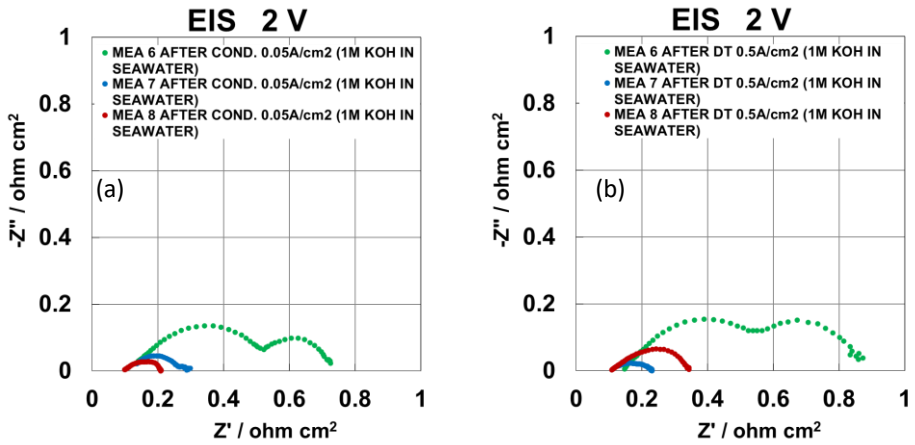

Figure 8. Nyquist plots of MEA 6, 7 and 8 measured after conditioning and after the durability test in seawater cathode configuration.

2.4.2 Electrochemical assessment of MEA 11

Figure 9 (a) reports the conditioning profile of MEA 11 characterised by 40% Pt/C (Thermo scientific) on Sigracet 10% with 0.81 mg/cm^2 loading at the cathode, Co_3O_4 (Alfa Aesar) onTi/Pt with 2.67 mg/cm^2 loading at the anode and PiperION® A40 operated at a constant current density of 0.1 A cm^{-2} and 50 °C, using 1 M KOH as electrolyte on both anode and cathode sides. The cell potential remains remarkably stable throughout the entire duration of the test, fluctuating within a narrow range around ~1.7–1.8 V. This behaviour indicates rapid stabilization of the electrode/membrane interfaces and efficient wetting of the catalyst layers. The absence of voltage drift or oscillations suggests that no significant activation processes, mass-transport limitations, or ohmic instabilities occur during this initial conditioning phase. Overall, the MEA exhibits excellent electrochemical stability under mild galvanostatic operation.

Figure 9 (b) compares the polarization curves of MEA 11 collected under different operating conditions: before conditioning and using 1M KOH as feed to both electrodes, after conditioning at 0.1 A cm^{-2} or 2 V and using 1M KOH in seawater at the cathode.

The data clearly show that conditioning improves the electrochemical response of the MEA. After conditioning in KOH, the polarization curve shifts toward lower cell voltages across the entire current density range, reflecting reduced activation and ohmic losses. Conditioning at 2 V results in an additional performance enhancement, likely associated with improved electrolyte penetration and removal of residual trapped gas within the porous structure. When 1M KOH in seawater was used at the cathode, the polarization curve shifted slightly upward, as expected, due to the presence of salts in seawater that interfere with OH^- ions causing issues in terms of transport and interfacial processes. Nevertheless, the MEA maintains good performance and stable operation, demonstrating robustness toward seawater-based electrolytes.

Figure 9 (c) shows the current response of MEA 11 during a potentiostatic conditioning step at 2 V and 50 °C, with 1 M KOH supplied to both electrodes. The current density gradually increases over time

before reaching a stable plateau. This progressive rise in current indicates ongoing activation of the electrode surfaces and improved ionic and mass-transport properties within the MEA. The trend suggests enhanced wetting of porous layers, better contact at the electrode membrane interfaces, and a reduction of any initial resistive contributions. The absence of current decay confirms that the MEA remains stable under high-voltage operation, without signs of degradation or catalyst deactivation.

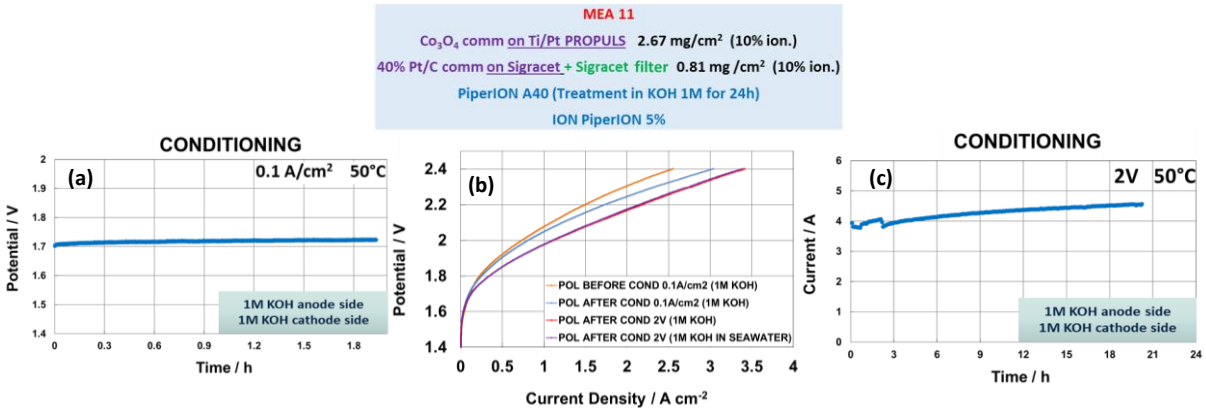

Figure 9. (a) Galvanostatic conditioning at 0.1 A cm^{-2} and 50 °C using 1 M KOH on both anode and cathode sides. (b) Polarization curves of MEA 11 collected before conditioning, after conditioning at 0.1 A cm^{-2}, after conditioning at 2 V, and after conditioning with seawater + 1 M KOH at the cathode. (c) Potentiostatic conditioning at 2 V and 50 °C in 1 M KOH.

As indicated above, conditioning at 2V results in an enhanced performance. Figure 10 presents the electrochemical impedance spectra of MEA 11 recorded at 1.5 V, 1.8 V, and 2.0 V under different operating conditions: before conditioning and using 1M KOH feed to both electrodes, after conditioning at 0.1 A cm^{-2} or 2 V and using 1M KOH feed to both electrodes, and after conditioning at 2 V when using 1M KOH in seawater at the cathode. All spectra exhibit a depressed semicircle typical of a charge-transfer-controlled process, allowing estimation of both the ohmic resistance (high-frequency intercept) and the charge-transfer resistance (diameter of the semicircle).

At 1.5 V (Figure 10 (a)) the MEA exhibits the largest impedance values among the three voltage conditions. The spectrum recorded before conditioning shows the highest overall semicircle, indicating substantial charge-transfer resistance and interfacial limitations at low overpotential. After conditioning and using KOH on electrodes, the impedance slightly decreases, reflecting improved wetting of the electrode layers and partial activation of catalytic sites. Conditioning at 2 V further reduces the impedance, which is consistent with enhanced accessibility of active sites and improved electrolyte distribution. When seawater + 1M KOH is used at the cathode, the semicircle increases again, suggesting additional kinetic and transport limitations associated with the presence of seawater ions. Overall, the EIS recorded at 1.5 V highlights the transition from an initially resistive interface to a more active electrode surface following conditioning.

At 1.8 V (Figure 10 (b)) the impedance decreases significantly compared to 1.5 V, indicating improved charge-transfer kinetics under higher overpotential. The spectrum measured before conditioning still shows the largest semicircle, while all three conditioning procedures produce a noticeable reduction in resistance and a leftward shift of the high-frequency intercept. This indicates lower ohmic losses

and faster interfacial kinetics. The influence of seawater is visible but moderate: the semicircle for MEA after conditioning and using seawater + 1M KOH at the cathode is slightly larger than those of the conditioned samples and measured with 1M KOH electrolyte feed, suggesting that seawater introduces additional interfacial resistance but does not compromise overall MEA stability. These results demonstrate that the benefits of conditioning become more pronounced as the cell moves into a more kinetically favourable regime.

At 2.0 V (Figure 10 (c)) all EIS spectra exhibit the smallest semicircles, reflecting highly activated conditions with low charge-transfer resistance. The MEA before conditioning displays the highest impedance within this voltage setting, but the difference compared to the conditioned states is significantly smaller than at 1.5 V. Conditioning in pure KOH produces the lowest overall impedance, confirming improved electrode membrane contact and optimized catalyst wetting. The seawater conditioning introduces only a slight increase in semicircle size compared to pure KOH, indicating a minor penalty associated with seawater-derived ions but no major degradation. The nearly overlapping high-frequency intercepts across all post-conditioning spectra confirm that the ohmic resistance remains relatively unaffected by the electrolyte composition.

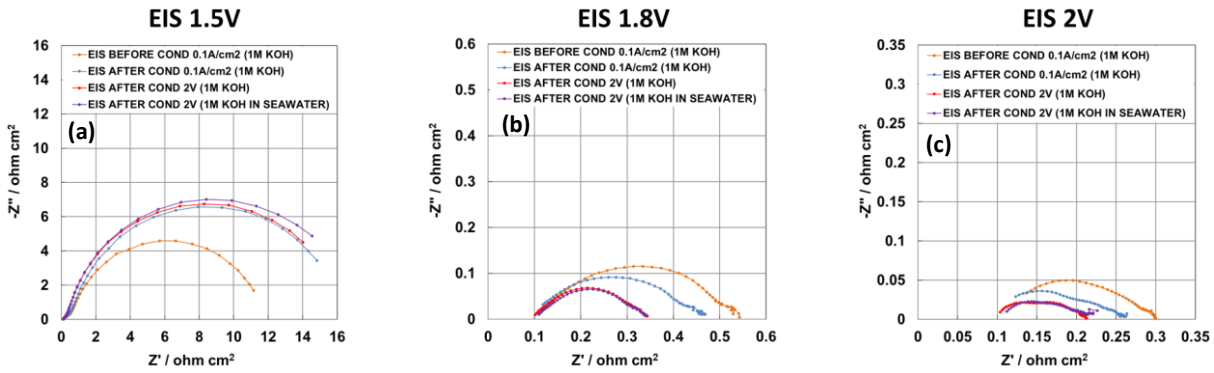

Figure 10. Electrochemical impedance spectra of MEA 11 measured at 1.5 V (a), 1.8 V (b), and 2.0 V (c) before and after conditioning in 1 M KOH or seawater + 1M KOH at the cathode.

2.4.3 Electrochemical assessment of MEA 12

MEA 12 had the same composition of MEA 11 but it was assessed under different conditions differing essentially for the conditioning procedure. Figure 11 reports the conditioning profile and the polarization performance of MEA 12, assembled with a Co_3O_4 anode catalyst (2.67 mg cm^{-2}), a Pt/C cathode (0.81 mg cm^{-2}), and a PiperION® A40 membrane previously treated in 1 M KOH. All measurements were performed at 50 °C using 1 M KOH at both electrodes, unless otherwise specified.

The conditioning curve (Figure 11 (a)) shows a gradual increase in cell voltage from approximately 1.65 V to 1.75 V over a 2.5-hour operation at 0.05 A cm^{-2}. This smooth upward trend indicates progressive deactivation of the electrode interfaces, likely due to a surface restructuring, change of catalyst wetting, and stabilization of the electrochemical double layer. The absence of oscillations or sharp variations confirms that MEA 12 operates in a stable regime throughout the conditioning step, with no evidence of gas blockage, flooding, or mass-transport instabilities. Compared to other MEAs

previously tested, MEA 12 exhibits a slightly lower performance, potentially reflecting the intrinsic activation dynamics of Co_3O_4 under alkaline conditions.

The polarization curves (Figure 11 (b)) demonstrate a consistent performance improvement after conditioning. The curve collected after conditioning and using 1M KOH as electrolyte feed shifts to lower voltages across the entire current density range, indicating reduced activation losses and improved membrane–electrode contact. This enhancement is particularly visible in the low-current region, where activation overpotentials dominate, confirming that conditioning effectively increases catalyst accessibility and optimizes ionic conduction within the electrode structure.

When the cathode is supplied with 1M KOH in seawater, the polarization curve exhibits only a slight voltage increase relative to pure KOH. This modest shift reveals that the presence of seawater salts introduces a small additional interfacial resistance but does not significantly hinder the overall electrochemical performance of the MEA. The stability of the polarization response indicates a good compatibility of MEA 12 with seawater-based electrolytes and suggests that the PiperION® membrane and Pt/C cathode maintain robust functionality even in the presence of more complex ionic compositions.

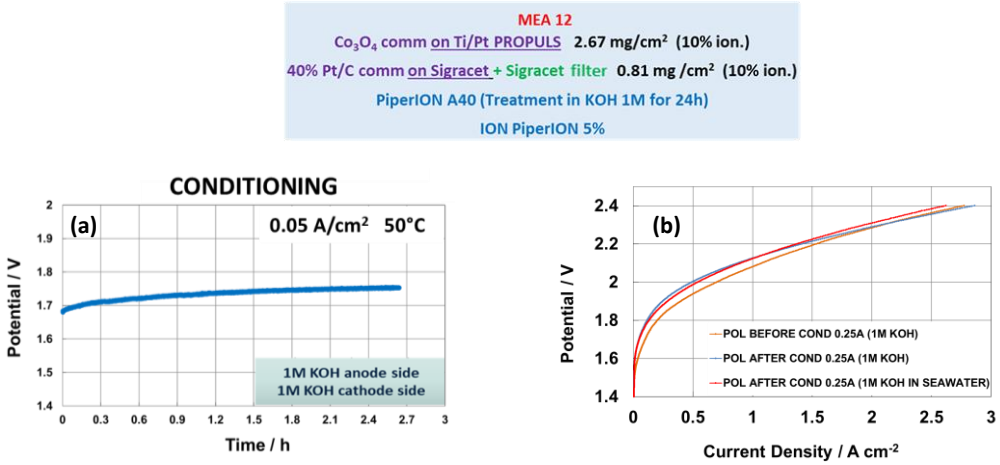

Figure 11. (a) Galvanostatic conditioning at 0.05 A cm^{-2} and 50 °C using 1 M KOH on both anode and cathode sides. (b) Polarization curves of MEA 12 collected before and, after conditioning using 1M KOH, and after conditioning when 1 M KOH prepared in seawater is used at the cathode.

Figure 12 presents the electrochemical impedance spectra of MEA 12 measured at 1.5 V, 1.8 V, and 2.0 V after different conditioning conditions: before conditioning and after conditioning at 0.05 A cm^{-2} applying 1M KOH electrolyte feed to both electrodes, and after conditioning at at 0.05 A cm^{-2} applying 1M KOH in seawater to the cathode. The three voltage conditions allow comparison of MEA behaviour from low-overpotential to highly activated regimes.

At 1.5 V (Figure 12 (a)), the impedance spectra show the largest semicircles, indicating that the electrode operates in a kinetic regime dominated by activation losses. The spectrum recorded before conditioning displays the highest overall resistance, with a large semicircle extending beyond 20 Ω cm², confirming a poorly activated interface. After conditioning and using 1M KOH as electrode feed, the semicircle decreases, showing improved charge-transfer kinetics and better catalyst utilization. When seawater+1M KOH is used at the cathode, the semicircle becomes slightly larger again, suggesting that

seawater introduces additional interfacial resistance, likely due to residual multivalent ions or altered ionic conductivity. Overall, the 1.5 V spectra highlight the substantial activation effect of conditioning and the moderate kinetic penalty associated with seawater operation.

At 1.8 V (Figure 12 (b)), the semicircles become significantly smaller (below 1 Ω cm^2), indicating that the MEA transitions into a more kinetically favourable regime. The spectrum of the MEA before conditioning remains the most resistive, but the difference between the conditioned states becomes much clearer: conditioning and testing in pure KOH leads to a significant reduction in charge-transfer resistance, conditioning and testing in seawater + 1M KOH produces only a slightly larger semicircle, meaning that seawater introduces a moderate but not severe interfacial limitation. The similarity in the high-frequency intercepts suggests that ohmic resistance (Rs) is nearly unaffected by seawater, and the main impact is on Rct or polarization resistance. Thus, at 1.8 V, MEA 12 shows stable operation and good resilience to seawater, with conditioning strongly enhancing performance.

At 2.0 V (Figure 12 (c)), all spectra show very small semicircles, confirming that MEA 12 is in a highly activated regime with low charge-transfer resistance. The curve for the MEA before conditioning still exhibits the largest semicircle, the one after conditioning and fed with KOH shows the lowest resistance, the one after conditioning and tested with seawater + 1M KOH shows only a minimal increase in Rct or polarization resistance. The nearly overlapping high-frequency intercepts indicate that Rs remains stable and nearly identical across conditions, while seawater causes only a slight kinetic penalty.

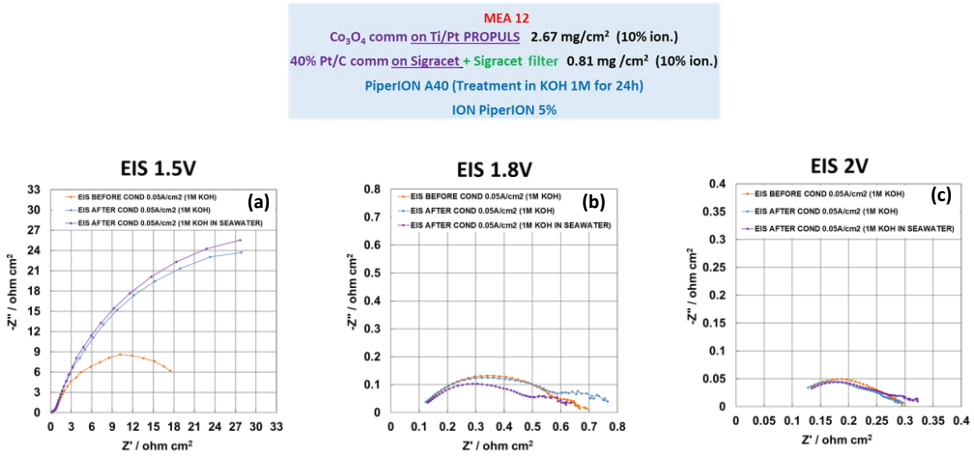

Figure 12. Electrochemical impedance spectra of MEA 12 measured at (a) 1.5 V, (b) 1.8 V, and (c) 2.0 V. Spectra are shown before conditioning tested with 1M KOH electrode feed, after conditioning at 0.05 A cm^{-2} and tested with 1M KOH feed, and after conditioning at the same current density and tested with 1M KOH + seawater cathode feed.

2.4.4 Electrochemical assessment of MEA 13

Figure 13 (a) shows the conditioning profile of MEA 13 assembled with a Co_3O_4 anode catalyst (2.67 mg cm^{-2}), a Pt/C cathode (0.83 mg cm^{-2}), and a PiperION® A40 membrane previously treated in 1M KOH operated at 0.05 A cm^{-2} and 50 °C using 1M KOH on both electrodes. The cell potential remains remarkably stable throughout the 1.7-hour activation period, fluctuating only between ~1.64 V and 1.70 V.

In contrast to carbon-based supports, the stainless-steel substrate leads to faster stabilization of electrode interfaces, reduced potential drift, and more uniform wetting behaviour. This suggests that stainless steel provides good mechanical contact and stable electronic conduction, which reduces the need for extended break-in. The stable profile also indicates that no detrimental corrosion or passivation phenomena occur during short-term operation in alkaline media at moderate current density.

Figure 13 (b) compares the polarization curves collected: before conditioning and after conditioning at 0.05 A cm^{-2} in 1M KOH electrode feed, after conditioning at 0.05 A cm^{-2} when seawater + 1M KOH is used at the cathode. After conditioning, the polarization curve shifts to slightly lower voltages, confirming improved catalyst utilization, better electrode membrane contact, and stabilization of ionic pathways within the electrode. The performance benefit is moderate but consistent across the entire current range, indicating efficient activation even with a metallic support. When the cathode is supplied with 1M KOH in seawater, the cell voltage becomes significantly higher, especially above 0.5 A cm^{-2}. This effect is more pronounced than in MEAs using carbon-based GDLs and suggests that: the stainless-steel support is more sensitive to seawater ions, interfacial charge-transfer resistance increases, and ionic/mass-transport limitations are enhanced at higher current densities. Unlike carbon substrates, stainless steel may interact differently with chloride-containing or high-salinity electrolytes, leading to slower kinetics on the cathode side when seawater-derived KOH is used.

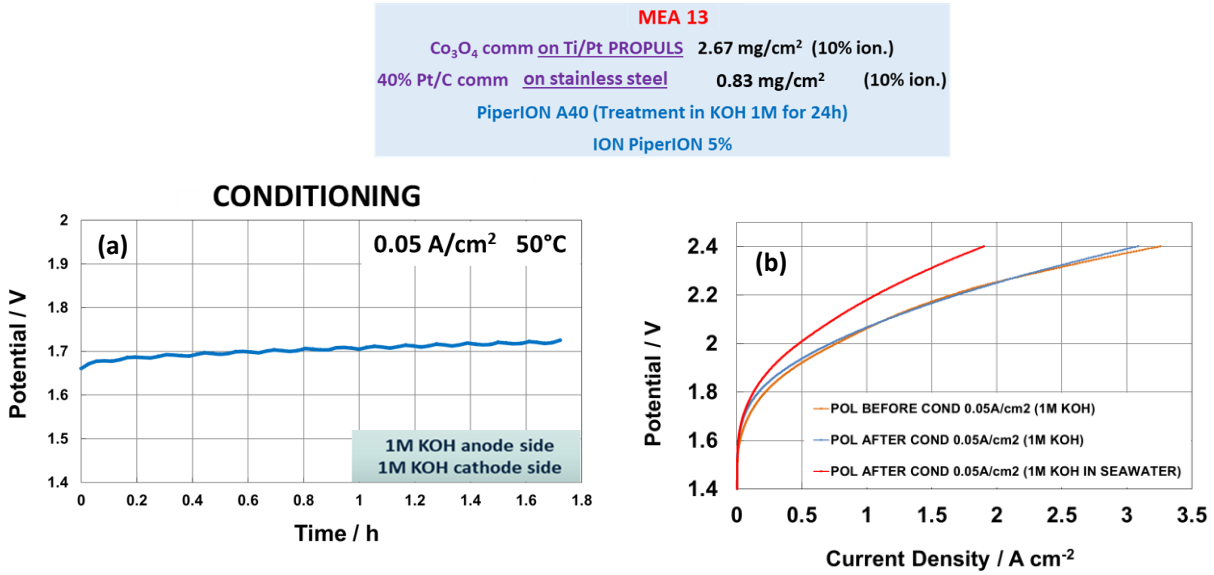

Figure 13. a) Galvanostatic conditioning at 0.05 A cm^{-2} and 50 °C tested in 1M KOH, showing a stable voltage profile with minimal drift, indicative of rapid interfacial stabilization on the stainless-steel support. (b) Polarization curves recorded before and after conditioning at 0.05 A cm^{-2} tested with 1M KOH electrode feed, and after conditioning at 0.05 A cm^{-2} with 1M KOH in seawater at the cathode.

Figure 14 (a) shows the largest semicircles are observed at 1.5 V, indicating dominant activation limitations at low overpotential. The spectrum before conditioning shows a smaller arc than the post-conditioning (KOH) case. This behaviour, also seen in other MEAs, suggests that break-in increases the electrochemically active surface capacitive contribution (CPE) and modifies interfacial structure such that, at low bias, the apparent loop can widen even if the interface is better wetted and activated. With seawater-derived KOH at the cathode, the semicircle increases substantially, pointing

to a marked rise in charge-transfer resistance (Rct) and/or mixed kinetic–transport penalties on the cathode side.

Figure 14 (b) shows the EIS spectra collected at 1.8 V; all arcs shrink by over an order of magnitude (≲1 Ω cm²), evidencing a transition to a more favourable kinetic regime. The MEA that was not subjected to conditioning remains the most resistive case; post-conditioning (with KOH electrolyte feed) delivers a smaller semicircle and a mild left shift of the high frequency (HF) intercept, consistent with lower Rct and slightly reduced Rs (better contacts/ohmic pathways). The seawater testing condition shows a moderately larger semicircle than pure KOH, with HF intercepts nearly overlapping the penalty is mostly kinetic/interfacial rather than ohmic.

At 2.0 V (Figure 14 (c)), all spectra display very small semicircles (≲0.3–0.4 Ω cm²), consistent with low Rct and efficient transport. The MEA that was not subjected to conditioning is still the most resistive, but the gap narrows compared with 1.5 V testing. Post-conditioning and testing in KOH yields the lowest impedance, while seawater introduces only a minor residual increase in Rct. HF intercepts remain very similar across conditions, confirming Rs ~ constant. Once fully activated, MEA 13 is robust; the seawater penalty persists but becomes small at high overpotential.

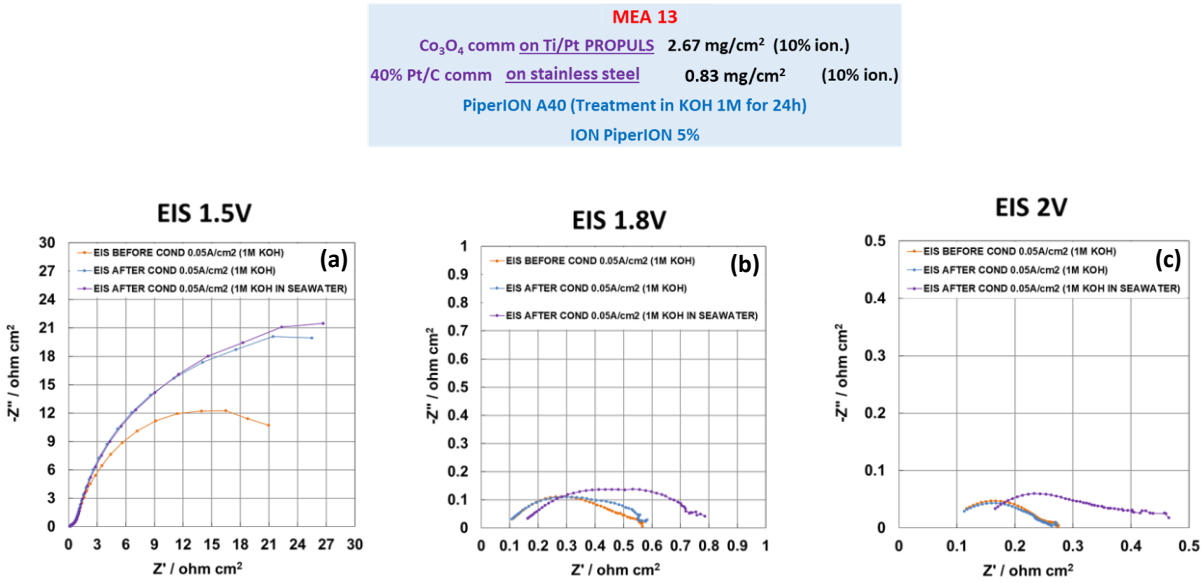

Figure 14. Electrochemical impedance spectra of MEA 13 measured at (a) 1.5 V, (b) 1.8 V, and (c) 2.0 V. Spectra are shown before and after conditioning at 0.05 A cm⁻² tested in 1M KOH, and after conditioning at 0.05 A cm⁻² with 1M KOH in seawater at the cathode.

2.4.5 Electrochemical assessment of MEA 15

Figure 15 summarizes the conditioning behaviour and polarization performance of MEA 15, assembled with a Co_3O_4 anode (2.55 mg cm⁻², 10 wt% ionomer) on Ti/Pt with an additional Ti/Pt filter, and a 40 wt% Pt/C cathode (0.81 mg cm⁻², 10 wt% ionomer) supported by Sigracet carbon paper and a stainless-steel filter. The PiperION® A40 membrane and ionomer were pre-treated in 1M KOH. All tests were conducted at 50 °C with 1M KOH supplied to both electrodes unless otherwise stated. Under galvanostatic conditioning at 0.05 A cm⁻², the cell voltage exhibits a flat and stable profile with only a slight upward drift over ~1.7 h. The absence of oscillations or spikes indicates rapid interfacial

stabilization, efficient wetting of the catalyst layers, and good ohmic contact across the assembly. The hybrid cathode architecture (Sigracet + stainless steel) likely combines the favourable gas liquid management of carbon paper with the uniform pressure distribution and robust electronic contact imparted by the metallic filter, thereby limiting break-in transients.

After conditioning of MEA and testing in 1M KOH the polarization curve shifts to lower voltages across the full current-density range, confirming reduced activation losses at low currents and improved ohmic/transport pathways at intermediate and high currents, Figure 15 (b). When 1M KOH in seawater is supplied at the cathode, the curve displays only a minor voltage penalty compared with post-conditioning in pure KOH. The difference is most evident in the low-to-mid current region and tends to compress at higher current densities, consistent with a small additional interfacial (kinetic) resistance introduced by the seawater-derived electrolyte while bulk ohmic contributions remain comparable. Overall, MEA 15 shows robust performance and limited sensitivity to seawater, supporting the idea of a synergistic effect: Sigracet preserves hydrophobic pathways and gas evacuation, whereas the stainless-steel filter stabilizes compression and electrical contact, promoting reproducible activation and minimal performance loss upon electrolyte change.

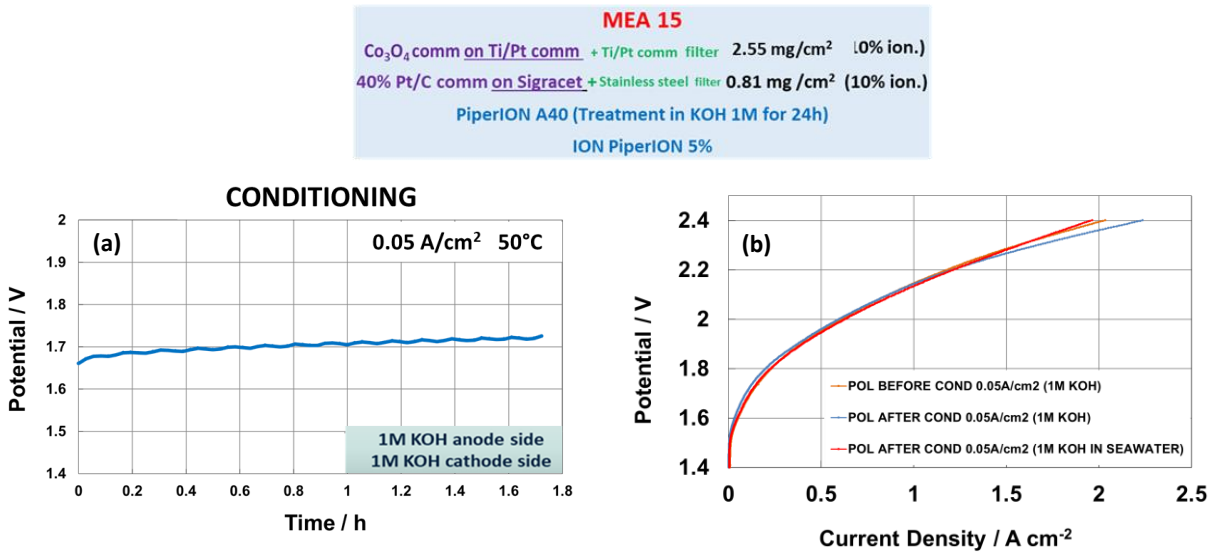

Figure 15. (a) Galvanostatic conditioning at 0.05 A cm^{-2} and 50 °C and testing in 1M KOH. (b) Polarization curves recorded before and after conditioning and tested in 1M KOH, and after conditioning and tested in 1M KOH in seawater at the cathode.

At 1.5 V (Figure 16 (a)) the impedance spectra of MEA 15 show relatively large semicircles, consistent with a regime dominated by activation losses and limited charge-transfer kinetics. The curve before conditioning exhibits the highest resistance, as expected for a non-activated interface. After conditioning in 1M KOH, the semicircle becomes visibly smaller, indicating improved wetting of the catalyst layers and enhanced catalyst utilization at the cathode. When seawater + 1M KOH is supplied at the cathode, the diameter of the semicircle increases compared with post-conditioning in pure KOH, but less dramatically than in MEAs using stainless steel alone. This suggests that the hybrid cathode structure (Sigracet + SS filter) helps buffering the kinetic penalty introduced by seawater ions, maintaining more favourable interfacial properties.

At 1.8 V (Figure 16 (b)) all semicircles shrink substantially, reflecting the move to a more kinetically favourable potential. The spectrum before-conditioning still shows the highest resistance, whereas conditioning produces a clear reduction in the charge-transfer resistance. The testing with seawater displays a slightly larger semicircle than that with pure KOH, but the relative difference is small, indicating that seawater introduces a moderate additional Rct calculation without altering the overall electrochemical behavior. The high-frequency intercepts remain close across conditions, suggesting that the ohmic resistance (Rs) is largely unaffected, and that seawater impacts predominantly the interfacial components.

At 2.0 V (Figure 16 (c)) the semicircles become very small (< 0.3–0.4 Ω cm²), confirming efficient charge-transfer kinetics and low interfacial resistance. Conditioning and testing in pure KOH leads to the lowest overall impedance, with the seawater-conditioned spectrum showing only a slightly larger loop. Notably, the curves overlap closely across the high-frequency region, indicating stable and nearly identical Rs, which confirms: good membrane hydration; robust cathode contact due to the presence of the stainless-steel filter, preservation of ionic conduction even with seawater. At high voltage, the seawater effect becomes minimal, demonstrating that MEA 15 behaves robustly under demanding operational conditions.

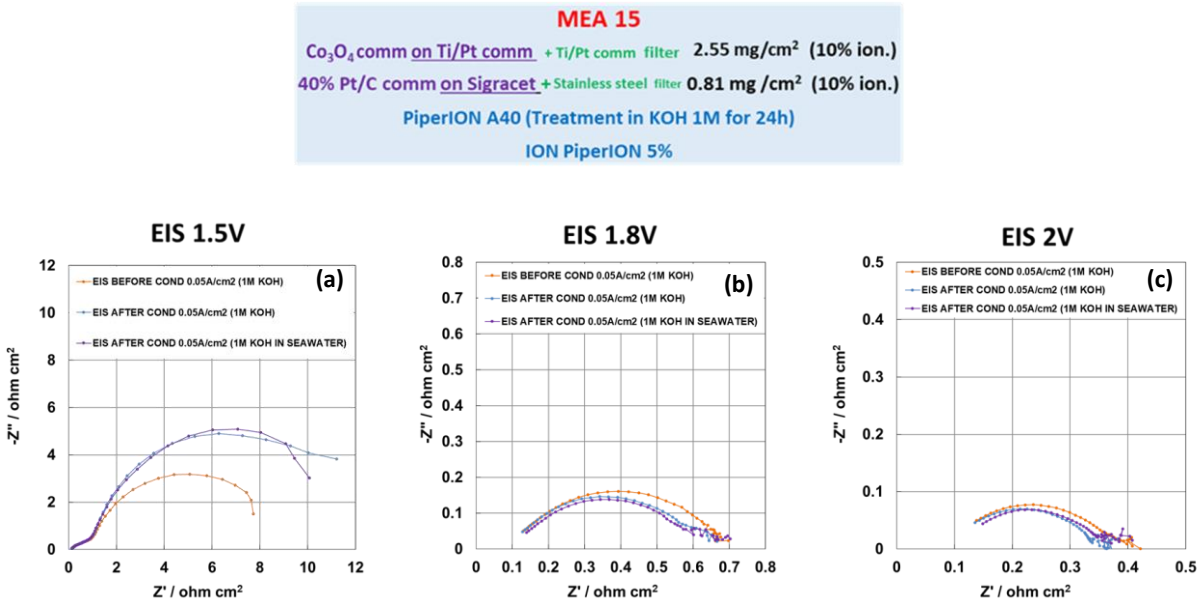

Figure 16. Electrochemical impedance spectra of MEA 15 measured at (a) 1.5 V, (b) 1.8 V, and (c) 2.0 V. Spectra are shown before conditioning and after conditioning at 0.05 A cm⁻² tested with 1M KOH, and after conditioning at 0.05 A cm⁻² and tested with 1M KOH in seawater at the cathode.

In summary, MEA 15 demonstrates strong electrochemical robustness and superior tolerance to seawater-derived electrolyte compared with other stainless-steel-based MEAs.

The polarization curves presented in the graph 17 show clear performance differences among the tested MEAs, and these trends can be directly related to the structural and compositional data reported in the corresponding table. Overall, the MEAs fall into two main performance groups. The best-performing membranes are those in the series MEA 11, 12, 13, and 15, all of which share a similar configuration: a Pt/C cathode supported on Sigracet, and a Co_3O_4 catalyst deposited on Ti/Pt at the

anode. These MEAs display the lowest voltages across the entire current density range, indicating both improved activation behavior at low current and reduced ohmic resistance in the mid-region of the curve. The very small differences within this group are likely due to slight variations in catalyst loading or the choice of filter materials, but the overall behavior remains consistent and robust. MEA 7 also shows relatively good performance and follows a trend similar to the best group, although with slightly higher voltages. This is consistent with its composition: it employs Pt/C at the cathode but uses Co_3O_4 on Ni-felt at the anode rather than Ti/Pt. The substitution of Ni-felt likely increases resistance and contributes to the modest performance penalty observed in the curve. A different behavior is observed in MEA 8, which uses NiFe LDH at the cathode and Ni-felt supports on both sides. This MEA performs at an intermediate level. The NiFe LDH catalyst improves the initial activation region relative to fully non-noble systems, but the metallic felt support and the absence of Pt still introduce additional resistive losses. Finally, MEA 6 shows the highest voltages and therefore the lowest overall performance. It uses a NiMo/KB cathode with a relatively high catalyst loading, combined with Co_3O_4 on Ni-felt at the anode. This fully non-noble configuration suffers both from less active oxygen evolution and hydrogen evolution catalysts and from higher ohmic contributions due to the choice of support. The result is a curve that remains consistently above the others throughout the whole current range.

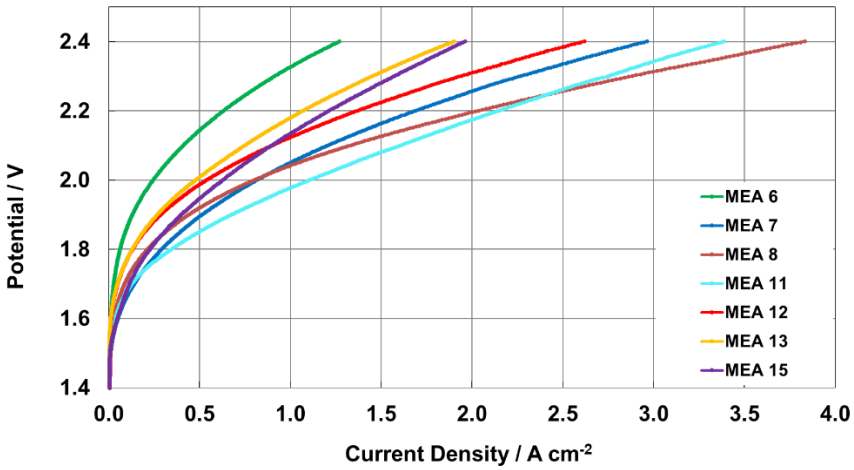

Figure 17. Polarization curves of all MEAs after conditioning in 1M KOH in seawater.

2.5 Half-cell catalyst screening at SINTEF

Catalyst screening studies often begin with aqueous model systems (AMS), such as rotating disk electrode (RDE) or bulk three electrode cells, as they allow rapid evaluation of activity and stability using minimal catalyst loading. However, these conventional AMS approaches employ thin, drop casted films that differ significantly from the gas transporting microporous structures used in real electrochemical cells. [4] As widely discussed in the literature, this structural mismatch means that catalyst behaviour observed in RDE type tests does not always translate to device level performance.

To address this gap, gas diffusion electrode (GDE) concepts were introduced in the 1990s as an intermediate testing platform and today there are a number of papers that do dedicated optimisation studies on the setup. [5] Within the SWEETHY project, SINTEF explored several different GDE holders and electrolyte supply setups in order to assess catalyst behaviour in a reproducible manner under alkaline water and alkaline seawater conditions.

2.5.1 First holder design: circular clamp-type holder with open front

The initial holder consisted of a circular cavity with a screw fastened cap and a gold contact ring positioned around the sample perimeter (Figure 18). This design intended to securely immobilize flexible freestanding samples, such as nano PTLs, during high current operation where vigorous bubble release can shake the sample and mechanically degrade the material. The cell body was machined from PEEK to prevent unintended reactions involving the housing materials.

Although this design delivered sufficiently high current responses, severe reproducibility issues emerged during testing for anodic seawater operation. The void space under the gold ring created stagnant zone that promoted severe crevice corrosion, causing rapid edge degradation of the samples within short operational periods (Figure 19).

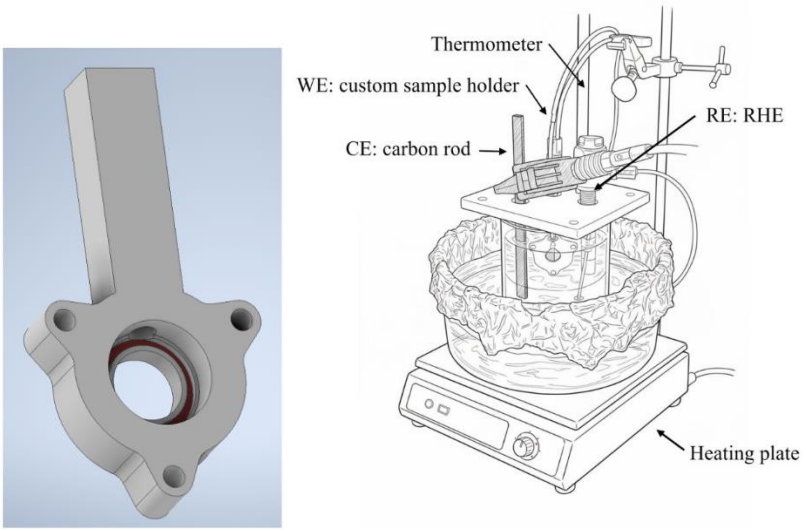

Figure 18. 3D representation of the sample holder (left) and experimental setup (right).

Figure 19. Nano PTL electrode before (left) and after (right) testing. The sample's edges are visibly damaged due to crevice corrosion taking place inside the sample holder shown in Figure 18.

In cathodic operation, crevice corrosion was not observed. However, large deviations between repeats persisted, preventing quantitative comparison. Judging from the irreproducible Linear Scan Voltammetry (LSV) results even in non-saline KOH conditions (Figure 20), irregular bubble accumulation within the porous substrate was suspected. The fully closed backside of the sample that limited gas escape pathway was also suspected to be a major factor. Chronopotentiometry at constant current density of 500 mA/cm^2 also did not show sufficiently reproducible results despite the steady state operation (Figure 21).

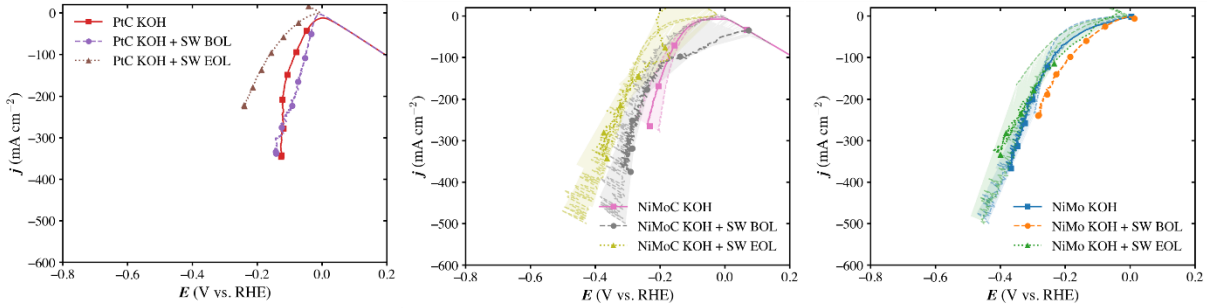

Figure 20. LSV for a PtC, NiMoC, and NiMo catalysts in KOH and KOH + seawater at the beginning and at the end of life. The shaded areas show the error derived from different measurements.

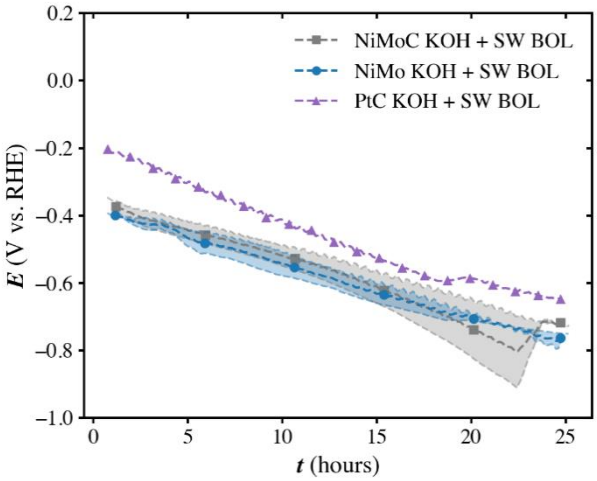

Figure 21. Chronopotentiometry of cathode catalyst samples conducted in alkaline synthetic seawater under constant current density of 500 mA/cm^2.

2.5.2 Second holder design: L-shaped holder with open front/back

The second design minimized crevice corrosion by reducing the clamping area to one edge of a square sample and enabling electrolyte and gas access on both front and back-side of the sample. Despite the modifications, reproducibility issues remained (Figure 22). We hypothesize that the primary constraint was the lack of controlled flow through the porous substrate, particularly given that PTFE-free carbon paper may not fully wet under immersion and short activation protocol, enabling irregular electrolyte intrusion and unpredictable bubble nucleation within the pores-free carbon paper.

Literature has shown that water and gas transport within unoptimized GDLs become unstable at low flow rates. For instance, a study on GDL hydrophilicity in PEMEL reported severe voltage fluctuations during constant-current operation at low flow rates, which stabilized only when sufficient flow was supplied. [6] The findings demonstrate that flow is essential to ensure consistent mass transport within GDLs, especially when the wettability or pore structure causes uncontrolled two-phase dynamics. This aligns with our observations, where run-to-run variability pertained in bulk testing setup and hindered reproducible electrochemical response.

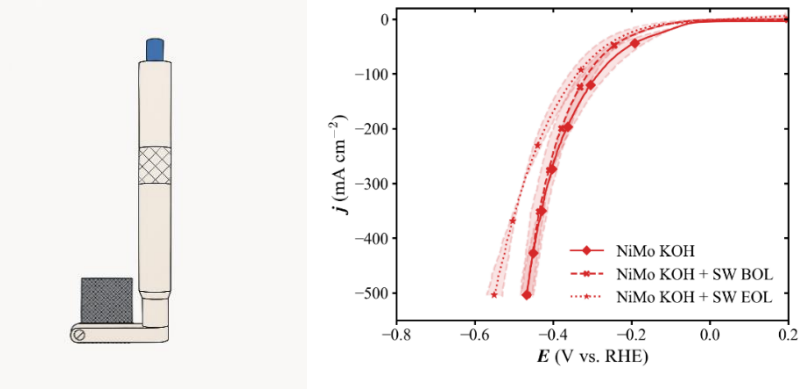

Figure 22. (left) Graphic representation of sample holder and (right) LSV for a NiMo catalyst in KOH and KOH + seawater at the beginning and at the end of life. The shaded areas show the error derived from different measurements.

2.5.3 Third holder design: immersed flow-type half-cell with gold-coated titanium plates

A third prototype incorporated gold-coated titanium flow/contact plates, PEEK end plates, and a PEEK membrane window separating the sample (working electrode) from the counter and reference electrodes. The entire assembly was immersed in electrolyte, allowing ionic conduction through the membrane (Figure 23). This design was chosen to mimic real cell architectures and to maintain uniform temperature, under the assumption that gold-coated titanium would remain relatively inactive toward OER or HER.

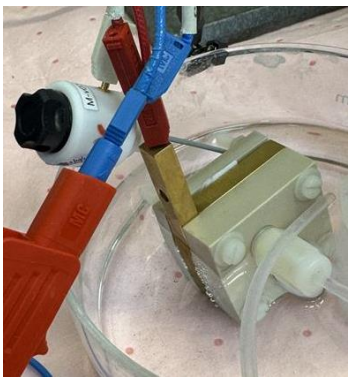

Figure 23. Photograph of the third holder design with flow, immersed in electrolyte for ionic conduction between reference and counter electrodes.

However, due to the small geometric area of the catalyst sample relative to the exposed area of the contact plates, the overall current density included significant contributions from the metallic contact plate exposed to the electrolyte. Visible discoloration after each experiment confirmed that parasitic reactions occurred on the contact plates. As a result, this configuration could not isolate catalyst performance from holder-induced artefacts.

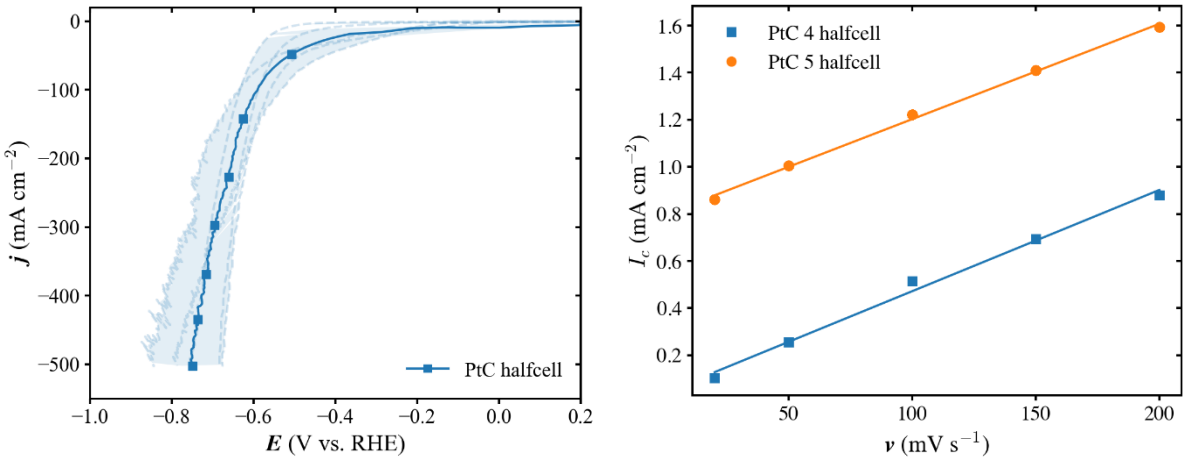

Figure 24. (left) LSV of PtC catalyst measured in the Au-coated Ti half-cell. As before, the shaded area represents the error, and it has been calculated as a result of multiple measurements. (right) Current as a function of voltage variation rate used to determine the electrochemical surface area.

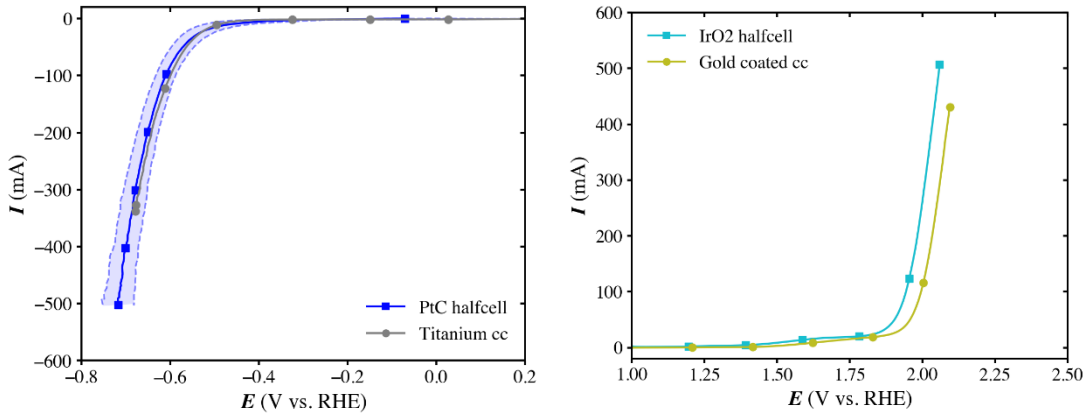

Figure 25. (left) LSV of flow half-cell using Ti current collector with and without PtC sample in 1M KOH. (right) LSV of flow half-cell using Au coated Ti current collector with and without IrO_2 sample in 1M KOH. Closely matching LSV indicates the overall current response is dominated by the current collectors, Ti particularly showing more dominant response in cathodic reactions.

Figures 24 shows that, although we find a comparable electrochemical surface area of ~ 100 cm^2 for the two samples, we still see high variability on the LSV curves. Additional LSV study was conducted on the half-cell without any sample in order to quantify the contribution of the half-cell component, particularly the Ti current collector (Figures 25). The result indicates that the Ti current collector is not inert in cathodic conditions in 1M KOH and may be the dominating contributor to variable current responses rather than the catalysts.

2.5.4 Fourth holder design: full flow-enabled reference cell configuration

The final design is a fully flow-enabled cell where electrolyte flows only through the active area, while the reference electrode is placed in a dedicated ionically conductive spacer compartment between the anode and cathode. Both sides of the reference compartment are separated from the working and counter compartments using membranes, forming a configuration as shown below in Figure 26. The configuration is a non-zero gap version of established reference electrode cells that enables real cell-like flow, minimized contact plate contribution, and deconvoluted monitoring of working and counter electrodes while avoiding complexities that can arise from reference electrode placement in zero gap reference electrode cell configurations, particularly due to bubbles and microfluidics issues.

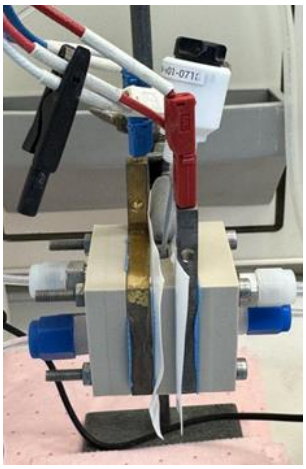

Figure 26. (left) Photograph of the fourth iteration holder/cell equipped with flow and compartment for reference electrode, (center) close-up photo of the reference electrode compartment, (right) fully assembled reference electrode cell in action.

The choice of separator for the reference-electrode compartment was optimized experimentally. PiperION® membrane, glass-fiber separators, and Celgard battery separators were evaluated for their ability to provide ionic conduction and maintain a flat, well-defined interface with the working electrode, similar to a full MEA configuration. Although using an AEM (membrane) offered real cell-like gas and flow management properties, it introduced a significant distortion in the high-frequency region of EIS response. HFR is essential for accurate iR-correction of catalyst activity. Cellgard porous separator had hydrophobicity issue that prevented good movement of electrolyte through the separator. Finally, glass fiber was selected for its thorough wettability that completely allowed ionic conduction without additional introduction of impedance.

Two essential steps were also included in the testing procedure:

1. Immersion of CCS in 1 M KOH prior to testing to ensure ionic conduction of ionomer;
2. Polishing the surface of titanium current collector prior to each test run to reset the conductivity of Ti.

After implementing all the improvements to the cell and the procedure, we were finally able to measure some reproducible and reliable results. Figure 27 shows three LSV curve measurements for HER using the cathode benchmark electrode, PtC. Ni felt was used as counter electrode. All the prepared SWEETHY catalysts will be screened using this final cell and the findings will be summarized in the following deliverable.

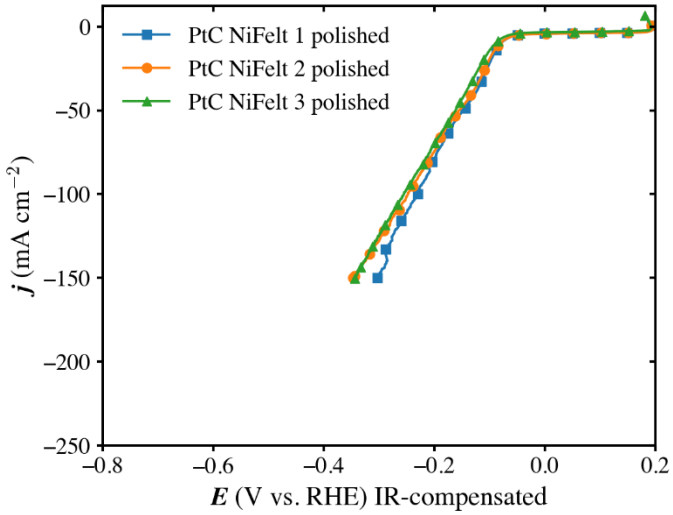

Figure 27. Three LSV results and for PtC benchmark cathode catalyst in 1M KOH, RT.

2.5.5 Testing conditions and protocols

The solutions used for the electrochemical measurements were (i) 1M KOH (ii) 1M KOH in synthetic seawater [2]. All measurements were run at a temperature of 50°C unless mentioned otherwise.

Table 3. Table of testing protocol used in screening task

Electrolyte	Technique	Notes
1M KOH	OCV	10 min
	PEIS	at OCV to check correct assembly
	ZIR	80% IR from HFR at 100 Hz and 0 V vs OCV
	CV	Conditioning: 30 cycles from 0.2 V to -0.8 V vs RHE at 50 mV/s
	LSV	0.2 V to -0.8 V at 1 mV/s
	PEIS	At -0.1, -0.3, -0.6 V vs RHE, from 200 kHz to 1 Hz
	ECSA	CV from –0.2 to 1.3 V vs RHE at 20, 50, 100, 150, 200 mV/s
	OCV	10 min
		Electrolyte change
1M KOH in seawater	OCV	10 min
	PEIS	at OCV to check correct assembly
	ZIR	80% IR from HFR at 100 Hz and 0 V vs OCV
	CV	Conditioning: 30 cycles from 0.2 V to -0.8 V vs RHE at 50 mV/s
	LSV	0.2 V to -0.8 V at 1 mV/s
	PEIS	At -0.1, -0.3, -0.6 V vs RHE, from 200 kHz to 1 Hz
	ECSA	CV from –0.2 to 1.3 V vs RHE at 20, 50, 100, 150, 200 mV/s
	OCV	10 min

2.5.6 Summary of methodological findings

Working with GDE architectures in the attempt of catalyst screening for seawater electrolysis introduced numerous challenges related to corrosion, two phase transport in porous media, and unwanted side reactions.

Consistent with the limitations reported for bulk GDE systems, we observed limitations from irregular electrolyte intrusion and bubble accumulation within the GDL. These hydrodynamic instabilities produced significant run-to-run variability, preventing reliable extraction of kinetic or stability metrics. The systematic troubleshooting ultimately led to the development of a flow-enabled simplified reference cell design and was therefore an essential step.

Final catalyst screening results will be included in the upcoming deliverable D3.3 First catalyst provision and data set on enhanced catalysts for direct operation with seawater

2.6 Three-electrode cell testing of PGM-free metal powder and self-standing electrocatalysts at CIDETEC

2.6.1 Hydrogen evolution reaction electrocatalysts

Testing procedure

Hydrogen evolution reaction (HER) performance was evaluated in a standard three-electrode cell (150 mL volume). HER electrocatalysts prepared by CIDETEC served as working cathode, a Pt wire in a glass porous frit acted as the counter anode, and a Hg|HgO|1M OH^- reference electrode equipped with a Luggin capillary was used. All the potentials were converted to the RHE scale.

Measurements were performed in either 1 M KOH or alkaline seawater (prepared according to [2]) using ultrapure water ($\kappa \leq 0.054$ µS/cm). The temperature was controlled at 25 ± 1 °C or 50 ± 1 °C with a recirculating thermostatic bath. The cell was deaerated with N_2 for 20 min prior to testing.

The testing protocol involved: (i) recording open-circuit potential (OCP) for 1 min; (ii) electrochemical impedance spectroscopy (EIS) from 10^5 to 1 Hz (10 points/decade, 5 mV amplitude); and (iii) three consecutive linear sweep voltammetry (LSV) scans at 1 mV/s for activity assessment. Tests were replicated on three samples. The LSV data were iR-corrected using R_u determined from EIS.

The testing was carried out for NiS_2 (both black and supported), MoS_2 (black and supported), $NiMoS_2$, and Mo_2C materials, as well as electrodeposited NiMo and NiMoS alloys, as previously reported in *Deliverable 3.1*. The catalyst's performance was compared to a benchmark Pt/C electrocatalyst.

- ***Nickel sulfide (NiS_2)***

Figure 288 shows the representative LSVs of NiS_2 black (black curves) and supported NiS_2 (red curves) versus a benchmark Pt/C electrocatalyst (40 wt. % Pt, blue curve) in 1 M KOH and alkaline seawater at 25 °C (a) and 50 °C (b).

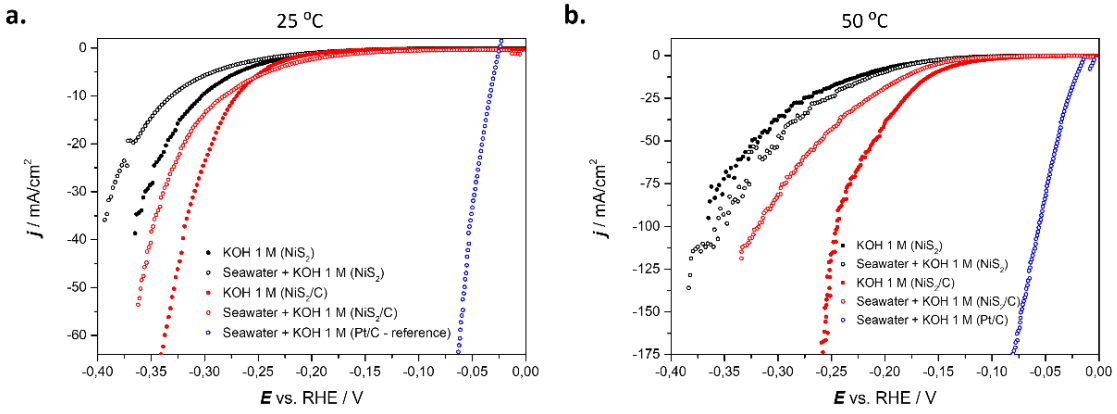

Figure 28. LSVs of NiS_2 black (in black), supported NiS_2 (in red) and Pt/C (benchmark, in blue) in KOH and alkaline seawater at 25 (a) and 50 (b) °C. The currents are normalized by geometric (projected) sample area.

Raising temperature to 50 °C accelerated kinetics across all samples, shifting curves to higher currents. Across both temperatures and electrolytes, the supported NiS_2 exhibits higher activity than the black material, likely due to an increased accessible surface area. In alkaline seawater, the HER activity of both materials decreases relative to KOH, possibly due to active-site poisoning by chloride ions. Chronopotentiometry measurements are planned to confirm these effects. Despite the improvements observed with support, both NiS_2 materials show HER activity significantly lower than the Pt/C reference.

- **Molybdenum- and Nickel-Molybdenum sulfides (MoS_2 and $NiMoS_2$)**

Figure 299 shows the LSVs obtained on MoS_2 black (black curves) and supported MoS_2 (red curves) versus benchmark Pt/C electrocatalyst (blue curve) in alkaline seawater at 25 °C (a) and 50 °C (b). The supported material demonstrates notably enhanced performance, presumably due to the increased active surface area. Nevertheless, the absolute HER activity remains low and substantially below that of the benchmark Pt/C electrocatalyst.

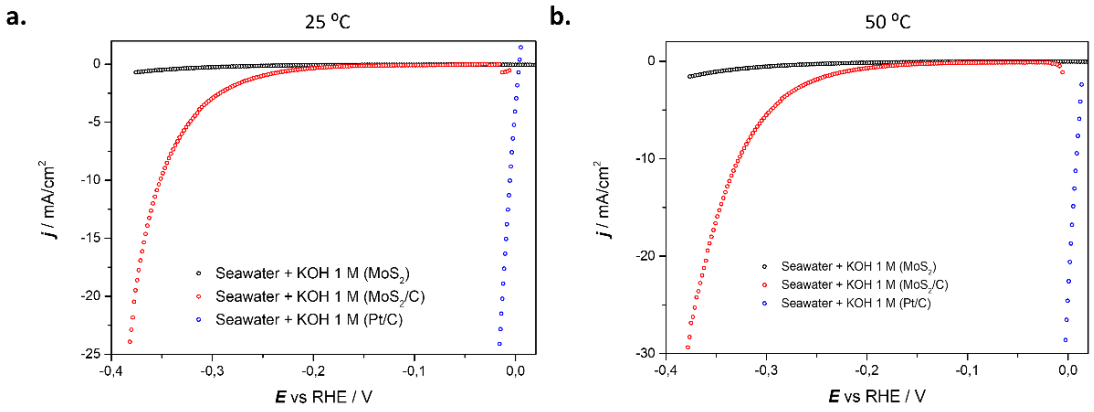

Figure 29. LSV of MoS_2 black (in black), supported MoS_2 (in red) and Pt/C (benchmark, in blue) in KOH and alkaline seawater at 25 (a) and 50 °C (b). The currents are normalized by geometric (projected) sample area.

Introduction of small amounts of nickel into MoS_2 leads to a significant improvement in catalytic activity, as shown in Figure 30. The LSVs of MoS_2 black (black curve) and $NiMoS_2$ (green curve) in alkaline seawater at 25 °C demonstrate a noticeable increase in current density for the Ni-modified material, alongside a significant decrease in the onset potential for HER.

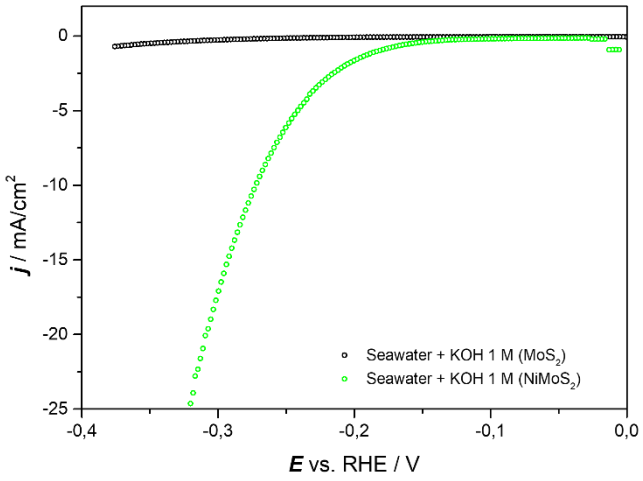

Figure 30. LSV of MoS_2 black (in black) and $NiMoS_2$ (in green) in alkaline seawater at 25 °C. The currents are normalized by geometric (projected) sample area.

- ***Molybdenum carbide (Mo_2C)***

Figure 31 presents the LSVs of Mo_2C/C electrocatalyst in 1M KOH and alkaline seawater at 25 and 50 °C. The Mo_2C/C electrocatalyst exhibits relatively low current densities across the investigated potential range. These results indicate limited HER activity under the tested conditions.

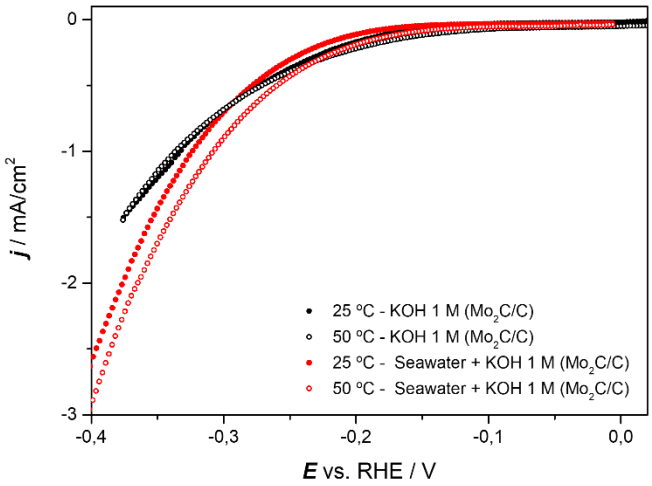

Figure 31. Representative LSV curves of Mo2C electrocatalysts tested in 1M KOH and alkaline seawater at 25 and 50 ºC. The currents are normalized by projected geometrical surface area.

- ***Electrodeposited Nickel-Molybdenum and Nickel-Molybdenum-Sulfur alloys (Ni-Mo and Ni-Mo-S)***

A systematic investigation of electrodeposited Ni-based catalysts for application in alkaline and seawater electrolysis was performed. The electrodes prepared under *Task 3.1.*2 *PGM-free self-standing cathode electrocatalysts*, Ni-Mo and Ni-Mo-S catalysts were initially electrodeposited on flat Cu substrates and evaluated for the HER in 1M KOH. Based on performance and durability, selected compositions were subsequently tested in alkaline seawater. The most promising formulations were then deposited onto carbon fiber substrates to produce high-surface-area HER electrodes for seawater operation.

Figure 32 shows the representative LSV curves obtained on the Ni-No and Ni-Mo-S alloys electrodeposited on flat Cu substrates. At 25 °C Ni-Mo-S samples consistently outperformed Ni-Mo counterparts, achieving higher geometric current densities. Raising temperature to 50 °C accelerated kinetics across all samples, shifting curves to lower potentials with Ni-Mo being more active.

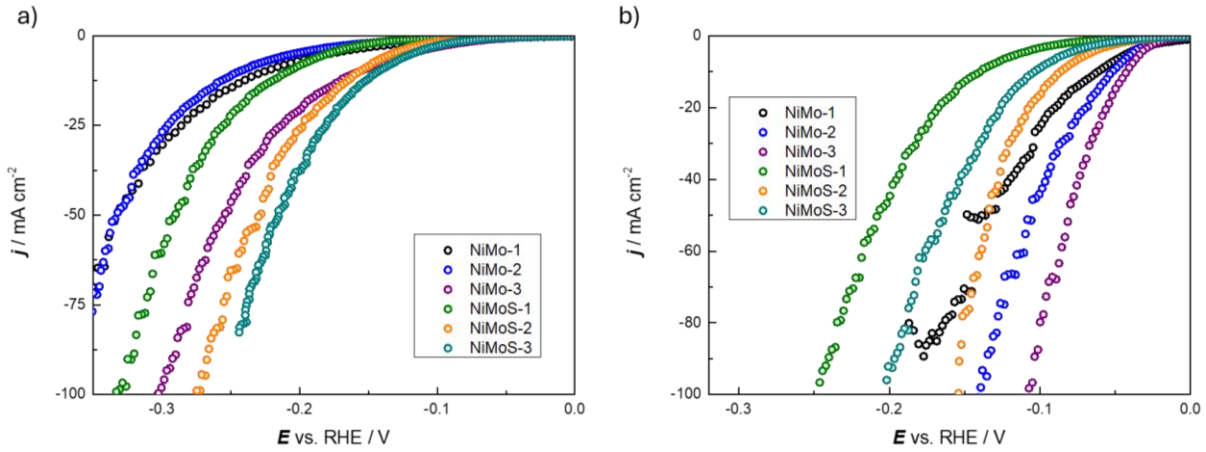

Figure 32. Representative LSV curves for Ni-Mo and Ni-Mo-S catalysts with variable composition (samples 1, 2, and 3) electrodeposited on flat Cu disks and tested in 1M KOH at (a) 25 and (b) 50 °C.

Following the initial screening of the electrodes in 1M KOH, one Ni-Mo alloy and two Ni-Mo-S alloys were selected for testing in alkaline seawater. Additionally, the selected electrodes underwent 500 LSV cycles in seawater-like conditions post-initial scan. Figure 33 shows that while the NiMoS-2 alloy shows the highest BoL activity, it degraded notably after dynamic cycling, suggesting Mo/S leaching or surface restructuring under Cl^- exposure. NiMo-3 and NiMoS-2 electrocatalysts showed minor degradation (small overpotential shift), with NiMo-3 outperforming in terms of achieved current densities.

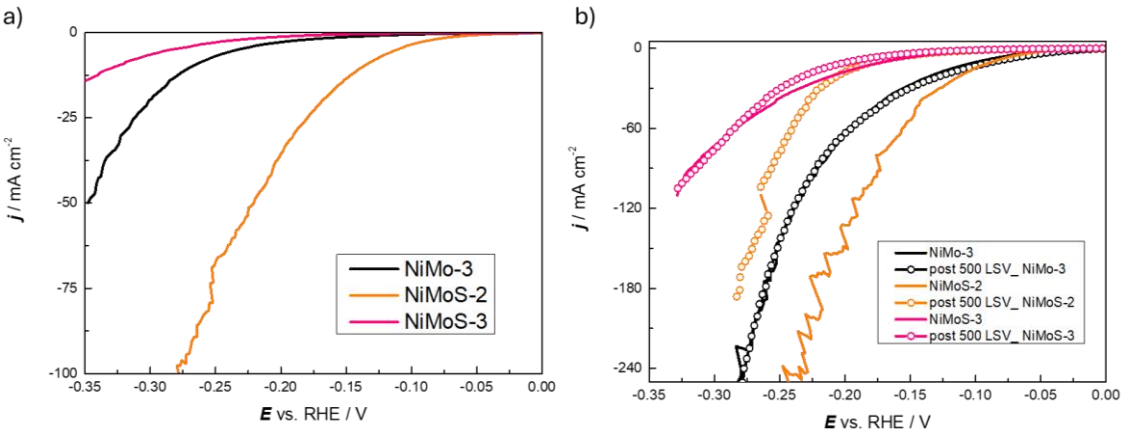

Figure 33. Representative LSV curves for Ni-Mo and Ni-Mo-S catalysts with variable composition (samples 1, 2, and 3) electrodeposited on flat Cu disks and tested in alkaline seawater at (a) 25 and (b) 50 °C.

The selected Ni-Mo and Ni-Mo-S electrocatalysts were electrodeposited on carbon fiber substrate (Freudenberg E20). Figure 34 demonstrates that at 25 °C and 50 °C, fiber electrodes delivered currents exceeding flat electrodes performance data, which is likely attributed to higher catalyst area, improved electrolyte access, and bubble management in the 3D scaffold. Similar trends are observed at 50 °C on fiber-coated substrate tested in seawater as compared to flat counterparts. Nevertheless, the effect of the fiber coverage on the obtained electrocatalysts performance needs to be investigated in more detail. The performance of the

Ni-Mo and Ni-Mo-S alloys was compared with the benchmark Pt/C cathode electrocatalyst. The data shown in Figure 34 demonstrate that the Pt-based electrocatalyst remains by far more active than the Ni-based non-noble alternatives.

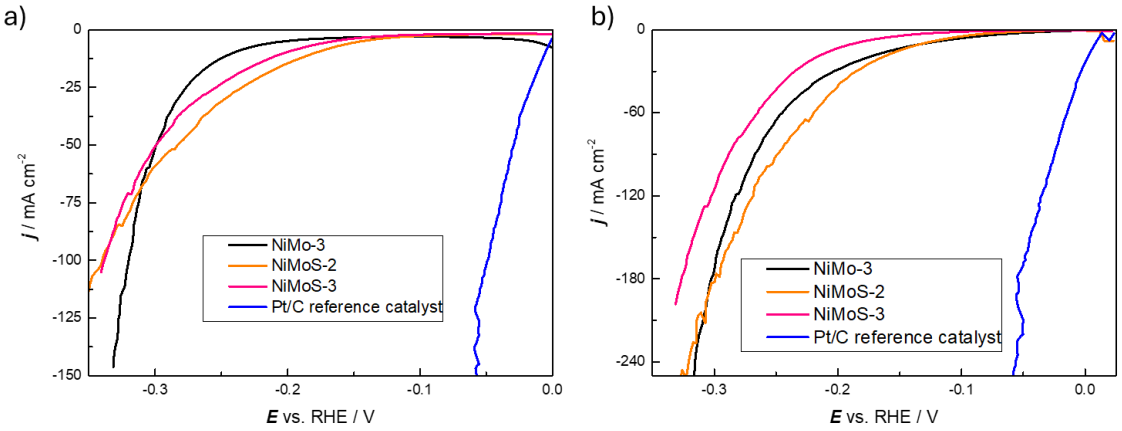

Figure 34. Representative LSV curves for NiMo and NiMoS catalysts electrodeposited on C fibers (Freudenberg E20) and tested in alkaline seawater at (a) 25 and (b) 50 °C. Currents are normalized by projected geometrical surface area.

2.6.2 Oxygen evolution reaction electrocatalysts

Testing procedure

Oxygen evolution reaction (OER) electrocatalysts were tested in the same three-electrode cell configuration as described in previous section, following the identical protocol for activity screening using LSV in the anodic potential window.

The LSV measurements were conducted on layered double hydroxide (LDH) materials, including NiFe-LDH and NiMn-LDH, as well as electrodeposited Ni-Mo and Ni-Mo-S alloys, as previously reported in [3]. The catalysts' performance was compared to a benchmark Co_3O_4 catalysts.

- **Nickel-Iron Layered Double Hydroxide (NiFe-LDH)**

Figure 35 shows the polarization curves of NiFe-LDH in both alkaline seawater and 1M KOH, compared against a benchmark Co_3O_4 electrocatalyst, tested at 25 °C and 50 °C. The data indicate enhanced electrocatalytic performance at elevated temperature for both electrolytes. When using seawater as an electrolyte, a slight decrease in activity is observed, likely due to active-site poisoning by chloride ions. This hypothesis will be further assessed through chronopotentiometric measurements. Compared with the reference electrode (shown in blue), the synthesized NiFe-LDH materials display slightly lower OER performance under the tested conditions.

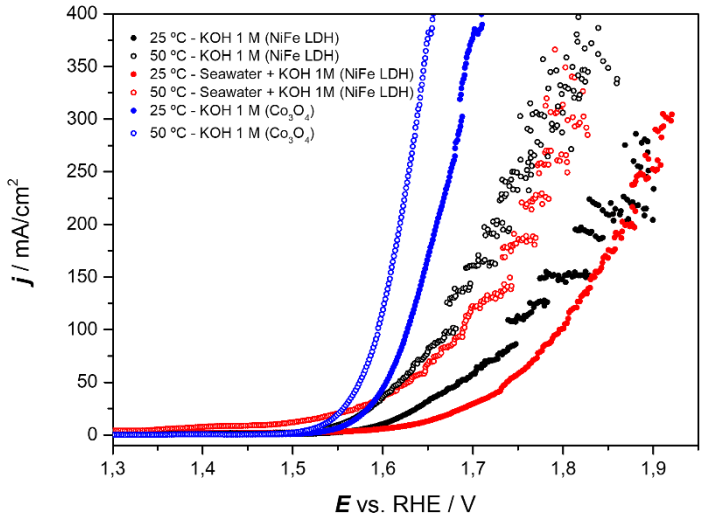

Figure 35. Representative LSV curves of NiFe-LDH and Co_3O_4 (benchmark) electrocatalysts tested in 1M KOH and alkaline seawater at 25 and 50 °C. The currents are normalized by projected geometrical surface area.

- **Nickel-Manganese Layered Double Hydroxide (NiMn-LDH)**

Figure 36 shows the polarization curves of NiMn-LDH in 1M KOH, compared with the benchmark Co_3O_4 electrocatalyst at 25 °C and 50 °C. The catalytic behavior of NiMn-LDH toward OER is comparable to that of the benchmark, particularly in terms of onset and overpotential, demonstrating its suitability as an alternative OER catalyst in alkaline media.

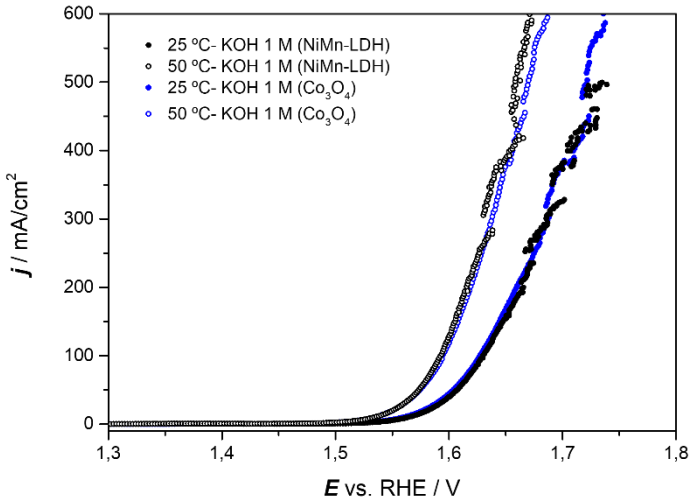

Figure 36. LSV of NiMn-LDH and Co_3O_4 (reference) in KOH and alkaline seawater at 25 and 50 °C. The currents are normalized by projected geometrical surface area.

- **Nickel-Molybdenum Oxide (Ni-MoO_3)**

Nickel-doped molybdenum oxide (approximately 7 wt. % Ni) was synthesized and characterized using LSV technique in both alkaline seawater and 1M KOH. The results are compared with benchmark Co_3O_4 electrocatalyst at 25 °C and 50 °C (Figure 37). While the Ni–MoO_3 material exhibits slightly lower OER performance than the Co_3O_4 reference, its activity remains relatively close. Notably, in alkaline seawater, catalytic activity decreases significantly.

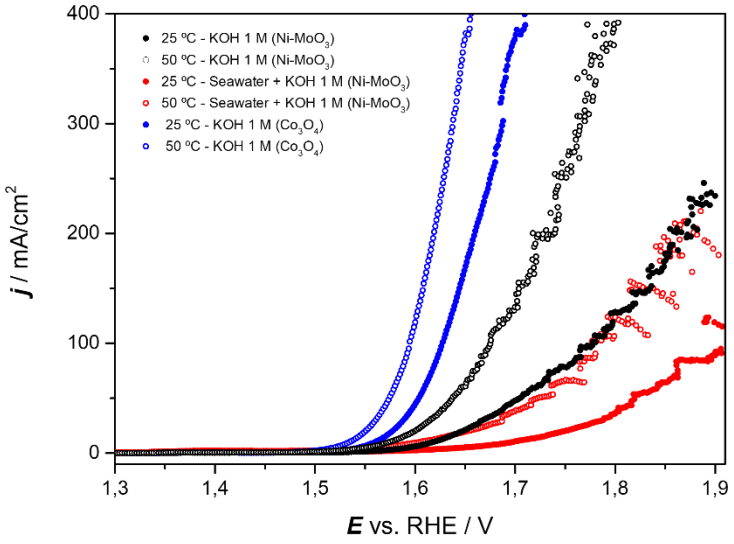

Figure 37. LSV of Ni-MoO_3 and Co_3O_4 (benchmark) in KOH and alkaline seawater at 25 and 50 °C. The currents are normalized by projected geometrical surface area.

- ***Electrodeposited Nickel-Molybdenum and Nickel-Molybdenum-Sulfur alloys (Ni-Mo and Ni-Mo-S)***

Ni-based catalysts prepared under *Task 3.2.2 PGM-free self-standing anode electrocatalysts* were evaluated for the OER, first on flat Cu substrates and subsequently on Ni felt to assess performance enhancement through 3D porous architectures. The tests were conducted in 1M KOH, which is fed to the anode side of the electrolysis cell.

The results in Figure 38 demonstrate that Ni-Mo-S generally outperforms Ni-Mo and reaches higher current densities at lower overpotentials, allowing them to attain higher current densities.

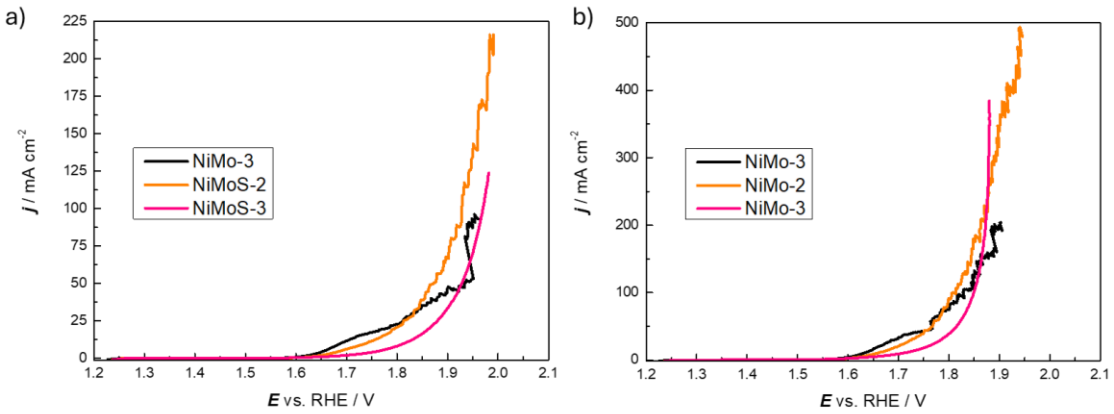

Figure 38. Representative LSV curves for Ni-Mo and Ni-Mo-S catalysts electrodeposited on flat Cu disks and tested in 1M KOH at (a) 25 and (b) 50 °C for OER.

Figure 39 demonstrates that when electrodeposited on porous Ni felt substrate, the OER currents are one order of magnitude higher than on Cu disks at the same potentials because of the much larger electrochemically active surface area. At 25 °C the Ni-Mo coating already shows substantial activity, but Ni-Mo-S delivers higher current densities at a given potential, indicating that sulfur incorporation and the tailored microstructure facilitate OER kinetics. Furthermore, the performance of Ni-based OER electrocatalysts was compared with benchmark Co_3O_4 electrocatalysts. The results shown in Figure 39 demonstrate that the activity of Ni-Mo-S alloy is comparable to the benchmark material.

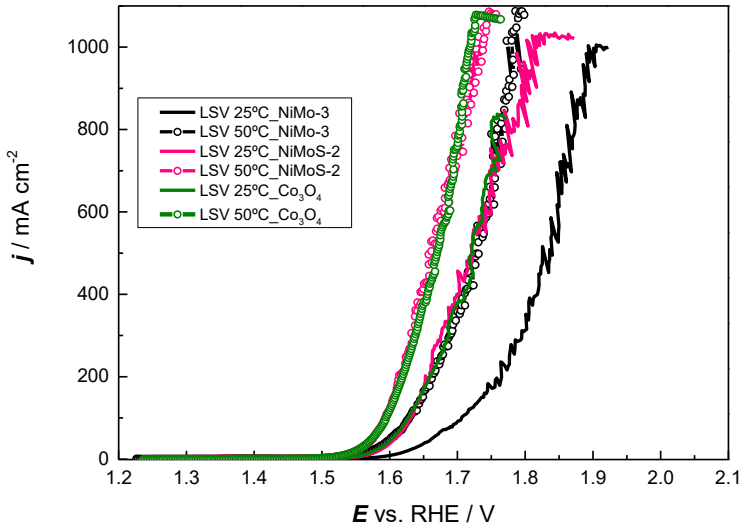

Figure 39. Representative LSV curves for NiMo and NiMoS catalysts electrodeposited on Ni felt substrate and tested in 1M KOH at 25 and 50 °C for OER. Currents are normalized by projected geometrical surface area.

3 Conclusions and recommendations

Across the full set of experiments obtained at **CNR** and performed on MEA 6, 7, 8, 11, 12, 13 and 15, a coherent picture emerges regarding the influence of catalyst composition, electrode supports, and electrolyte nature on the operation of an AEM-based water electrolyzers with seawater. The combined analysis of conditioning behaviour, polarization curves and impedance spectra shows that all MEAs benefit significantly from an initial activation period, which improves catalyst wetting, strengthens interfacial contact, and reduces both ohmic and charge-transfer losses. In most cases, conditioning results in more stable cell potentials and a clear downward shift in the polarization response, confirming that proper hydration and ionic equilibration of the ionomer and membrane are essential for achieving optimal electrochemical activity.

The comparison among different catalyst systems confirms a significant role of the anode in determining Ir-free alkaline water electrolysis performance. MEA 8, equipped with NiFe-LDH, consistently outperforms Co-based analogues both before and after conditioning, demonstrating intrinsically faster OER kinetics. MEAs employing commercial Co_3O_4 (MEA 11–15) exhibit robust and reproducible behaviour, especially when electrode architecture is optimized. These systems also demonstrate that high performance can be maintained even in the absence of noble-metal anodes, provided that interfacial properties are properly managed. On the other hand, Pt outperforms NiMo as expected but this has a negative impact on sustainability.

A key result of the study concerns the impact of cathode support materials. Carbon-based supports, such as Sigracet, offer excellent gas evacuation and favourable wetting, while stainless steel provides mechanical robustness but shows higher sensitivity to seawater-derived electrolytes. Hybrid assemblies, such as the one used in MEA 15 (Sigracet combined with a stainless-steel filter), strike an effective balance: they ensure stable conditioning, maintain low cell voltages after activation, and limit the performance penalty associated with seawater electrolytes. This highlights the importance of considering not only catalyst materials, but also the structural and transport properties introduced by the support layers.

The use of 1M KOH prepared in seawater introduces a moderate but consistent kinetic penalty, observed mainly as a slight increase in charge-transfer resistance and a small upward shift in polarization curves. Importantly, the ohmic resistance remains largely unchanged, indicating that seawater affects predominantly interfacial processes rather than bulk ionic conduction. At higher voltages (1.8-2.0 V), all MEAs experience a transition into a highly activated regime where impedance loops shrink and differences between conditions compress, demonstrating that seawater operation is viable, especially at elevated current densities.

Overall, the results show that MEAs based on PiperION® membranes can operate successfully in both pure KOH and alkaline seawater electrolytes, provided that appropriate electrode architectures are used. The combination of optimized catalyst layers, effective conditioning, and hybrid support structures enables stable, efficient, and seawater-tolerant operation. Taken together, these findings offer a solid foundation for the development of cost-effective and robust AEM electrolyzers for applications where seawater-based alkaline feeds are advantageous or necessary.

SINTEF studies regarded catalyst evaluation in half-cell using a gas diffusion electrode (GDE). Several different GDE holders and electrolyte supply setups were explored to assess catalyst behaviour in a reproducible manner under alkaline water and alkaline seawater conditions. The results in half-cell are essentially on-line with those observed at CNR with PGM electrocatalysts (e.g. Pt-based) showing better performance and durability compared to the PGM free systems (e.g. NiMo based). The same evidences have been observed at CIDETEC (see below).

On the other hand, a comprehensive evaluation of non-noble electrocatalysts for HER and OER was carried out in a three-electrode configuration at **CIDETEC** using alkaline (1M KOH) and seawater electrolytes, with benchmarking against Pt/C and Co_3O_4 reference catalysts. For HER, sulfide-based catalysts (NiS, MoS_2, NiMoS) exhibited stable and sustained activity in seawater conditions. Catalyst support integration and Ni-modified MoS_2 significantly reduced onset potentials and enhanced current densities, demonstrating the beneficial role of compositional and structural tuning. In addition, self-supported cathodes fabricated via electrodeposition of NiMo and NiMoS alloys onto carbon substrates showed pronounced HER performance in seawater. While NiMoS alloys achieved higher current densities compared to NiMo, they experienced accelerated degradation, highlighting a clear trade-off between catalytic activity and operational stability.

On the anode side, layered double hydroxides (NiFe-LDH and NiMn-LDH) together with NiMo oxides delivered robust OER activity comparable to the Co_3O_4 benchmark, particularly in alkaline media. Moreover, electrodeposited, self-standing NiMoS electrocatalysts on porous Ni felt achieved high current densities, matching benchmark performance and surpassing it in absolute current output due to enhanced surface area and the synergistic effect of sulfur incorporation.

Overall, these Ni-based materials demonstrate strong potential as cost-effective alternatives for seawater electrolysis. Future work will focus on extended durability testing and long-term stability assessments to validate their practical applicability under industrially relevant operating conditions.

4 Risks and interconnections

With regard to WP3 of the SWEETHY project, occurrence of insufficient stability of non-CRM electrocatalysts for direct seawater operation was identified as a risk. This aspect was carefully considered and durability tests have been carried out in this regard. Under specific conditions, in the presence of coated PTLs, the electrocatalysts show reasonable stability at the moment. After a conditioning period, the degradation rate in single cell is not significantly different from that observed in conventional AEM electrolysis. However, these aspects need to be explored more in depth and durability tests covering a reasonable period of time will be reported in the following Deliverable 3.3. As mitigation strategy, PGM and CRM based electrocatalysts have been explored as back-up solution showing relatively good stability.

No unforeseen risks were identified nor they appeared so far.

This report describes further the catalysts developed in WP3 of the SWEETHY project. The previous report **D3.1 "Catalysts preparation and characterisation for direct operation with seawater**" was published in M10 of the project (December 2025). The upcoming **D3.3 "First catalyst provision and data set on enhanced catalysts for direct operation with seawater"** (sensitive deliverable) in M16 of the SWEETHY project (June 2026) will report on durability results of the catalysts.

5 Acknowledgement

The author(s) would like to thank the partners in the project for their contributions and reviewing of the document.

Project partners:

#	Partner short name	Partner Full Name
1	RISE	RISE RESEARCH INSTITUTES OF SWEDEN AB
2	CNR	CONSIGLIO NAZIONALE DELLE RICERCHE
3	CIDETEC	FUNDACION CIDETEC
4	DLR	DEUTSCHES ZENTRUM FUR LUFT- UND RAUMFAHRT EV
5	IC	INSTITUT DE LA CORROSION SASU
6	SINTEF	SINTEF AS
7	PROPULS	PROPULS GMBH
8	CENMAT	CUTTING-EDGE NANOMATERIALS CENMAT UG HAFTUNGSBESCHRANKT
9	UNR	UNIRESEARCH BV

6 References

[1] Campagna Zignani, S.; Salanitro, A.; Pascale, M.; Fazio, M.; Aricò, A.S. Cell preservation strategies in direct seawater electrolysis based on cost-effective anion exchange membrane technology, Electrochimica Acta 2025, 530, 146406, https://doi.org/10.1016/j.electacta.2025.146406.

[2] D7.1 Single-cell test specification. https://sweethy.eu/deliverables/.

[3] D3.1 Catalysts preparation and characterisation for direct operation with seawater https://sweethy.eu/deliverables/.

[4] Fan, J.; Chen, M.; Zhao, Z.; Ye, S.; Xu, S.; Wang, H.; Li, H. Bridging the Gap between Highly Active Oxygen Reduction Reaction Catalysts and Effective Catalyst Layers for Proton Exchange Membrane Fuel Cells. Nat. Energy 2021, 6 (5), 475–486. https://doi.org/10.1038/s41560-021-00824-7.

[5] Reichmann, I.; Lloret, V.; Ehelebe, K.; Lauf, P.; Jenewein, K.; Mayrhofer, K. J. J.; Cherevko, S. Scanning Gas Diffusion Electrode Setup for Real-Time Analysis of Catalyst Layers. ACS Meas. Sci. Au 2024, 4 (5), 515–527. https://doi.org/10.1021/acsmeasuresciau.4c00018.

[6] Il Jang, T.; Ho, G. C.; Ri, H. M.; Hong, S. Hydrophilic Treatment of Carbon Paper for Anodic Porous Transport Layer in Proton Exchange Membrane Water Electrolyzer. React. Kinet. Mech. Catal. 2025, 138 (1), 221–233. https://doi.org/10.1007/s11144-024-02720-z.

[7] European Commission. Joint Research Centre. Hydrogen Production via Direct Seawater Electrolysis.; Publications Office: LU, 2025.

Disclaimer/ Acknowledgment

The project is supported by the Clean Hydrogen Partnership and its members.
Co-funded by the European Union under Grant Agreement No. 101192342. The views and opinions expressed are those of the author(s) only and do not necessarily reflect those of the European Union or the Clean Hydrogen Partnership. Neither the European Union nor the granting authority can be held responsible for them.